remote sensing

MDPI

Article

A Multi-Temporal Sentinel-2 and Machine Learning Approach for Precision Burned Area Mapping: The Sardinia Case Study

Claudia Collu [1,2,*], Dario Simonetti [3], Francesco Dessì [1], Marco Casu [1,2], Costantino Pala [1] and Maria Teresa Melis [1]

[1] Department of Chemical and Geological Sciences, University of Cagliari, 09042 Monserrato, Italy; fdessi@unica.it (F.D.); marco.casu4@unica.it (M.C.); costantino.pala@unica.it (C.P.); titimelis@unica.it (M.T.M.)
[2] Department of Civil, Constructional and Environmental Engineering, Sapienza University of Rome, 00184 Rome, Italy
[3] Independent Researcher, 21100 Varese, Italy; gis.dario.simonetti@gmail.com
* Correspondence: claudia.collu@uniroma1.it

Highlights

What are the main findings?

- A locally calibrated method for mapping burned areas (BAs) in Mediterranean environments was developed using Sentinel-2 MSI time series, integrating spectral, temporal, and topographic information within Google Earth Engine.
- The model achieved a Dice Coefficient of 91.8%, significantly outperforming existing regional (EFFIS) and global (MODIS, CLMS) burned area products, especially for small and fast-recovering fires.

What are the implications of the main findings?

- The proposed approach enables accurate, high-resolution, and consistent annual burned area mapping, supporting long-term wildfire monitoring and vegetation recovery assessment.
- The workflow is transferable to other Mediterranean or fire-prone regions, offering an operational and scalable tool for environmental monitoring, land management, and climate-related fire impact studies.

Abstract

The escalating threat of wildfires under global climate change necessitates rigorous monitoring to mitigate environmental and socio-economic risks. Burned area (BA) mapping is crucial for understanding fire dynamics, assessing ecosystem impacts, and supporting sustainable land management under increasing fire frequency. This study aims to develop a high-resolution detection framework specifically calibrated for Mediterranean environmental conditions, ensuring the production of consistent and accurate annual BA maps. Using Sentinel-2 MSI time series over Sardinia (Italy), the research objectives were to: (i) integrate field surveys with high-resolution photointerpretation to build a robust, locally tuned training dataset; (ii) evaluate the discriminative power of multi-temporal spectral indices; and (iii) implement a Random Forest classifier capable of providing higher spatial precision than current operational products. Validation results show a Dice Coefficient (DC) of 91.8%, significantly outperforming the EFFIS Burnt Area product (DC = 79.9%). The approach proved particularly effective in detecting small and rapidly recovering fires, often underrepresented in existing datasets. While inaccuracies persist due to cloud cover and landscape heterogeneity, this study demonstrates the effectiveness of a machine learning approach for long-term monitoring, for generating multi-year wildfire inventories, offering

Academic Editor: Carmen Quintano

Received: 26 November 2025
Revised: 30 December 2025
Accepted: 13 January 2026
Published: 14 January 2026

a vital tool for data-driven forest policy, vegetation recovery assessment and land-use change analysis in fire-prone regions.

Keywords: burned area mapping; Sentinel-2 MSI; time-series analysis; wildfire monitoring; machine learning

1. Introduction

Wildfire represents one of the major ecological disturbances at the global scale, with significant impacts on ecosystems, climate, and human societies. These events, either natural or anthropogenic, involve the uncontrolled combustion of vegetation, leading to loss of biodiversity, alteration in biogeochemical cycles, and the release of large amounts of greenhouse gases and aerosols into the atmosphere. Moreover, wildfires can be considered a causative factor for the triggering of postfire debris-flows [1]. Over the past decades, rising temperatures, prolonged droughts, and land-use changes linked with urbanization have contributed to increasing fire frequency, duration, and severity worldwide [2–5].

In the Mediterranean Basin, wildfires are a recurrent and structural phenomenon, strongly influenced by hot and dry summers, flammable vegetation, intense winds, and extensive land abandonment, which increases fuel load [6–8]. According to data from the European Forest Fire Information System (EFFIS), southern Europe has experienced a marked increase in burned areas in recent years, with longer and more intense fire seasons. Within this critical regional context, Italy ranks as the fourth European country most impacted by wildfires in 2024 (Figure 1). Significantly, the island of Sardinia stands out as one of the most fire-affected regions in Italy [9], where fires of varying size and severity occur every year, causing substantial environmental, economic, and social damage.

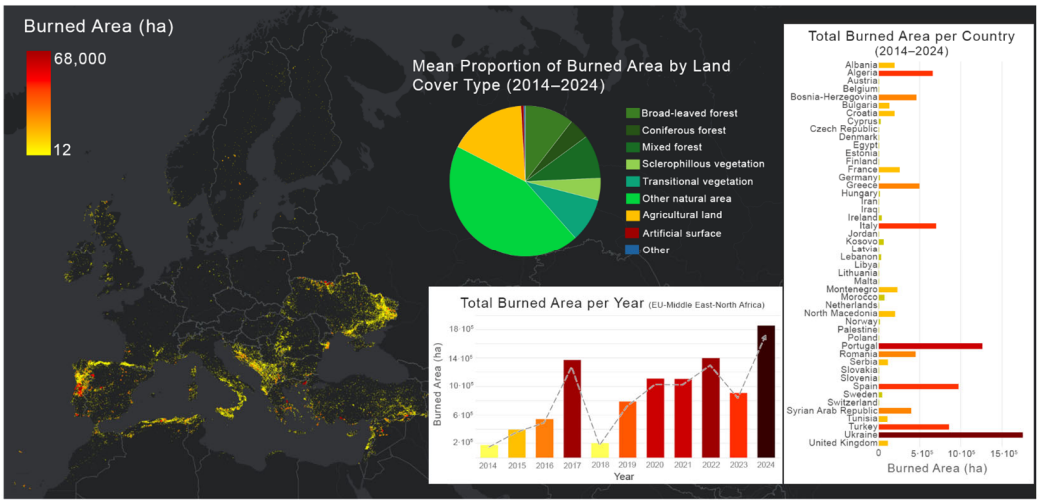

Figure 1. Wildfire activity and burned area distribution across Europe, Middle East and North Africa (2014–2024), according to the European Forest Fire Information System (EFFIS). The map shows the spatial distribution of wildfire events over the last decade, with point color intensity indicating burned area extent (in hectares). On the upper center, the average proportion of burned area by land-cover type highlights the dominant vegetation classes affected by fires. The lower central panel illustrates the annual total burned area across Europe, Middle East and North Africa, revealing an overall increasing trend (grey dash line arrow) culminating in 2024, the year with the largest extent of burned surfaces. On the right, total burned area per country over the 2014–2024 period is reported (bar colors represent burned area magnitude, with a gradient from yellow to dark redshowing that Italy, particularly its southern regions, ranks among the most severely affected areas in Europe.

Accurate mapping of burned areas (BAs) is essential for quantifying the spatial extent and distribution of fires, estimating carbon emissions, and supporting recovery, prevention, and land management strategies. Remote sensing provides an effective means to detect and monitor burned areas, offering synoptic, frequent, and multi-temporal observations [10–13]. Vegetation scars produced by fire events cause substantial alterations in the spectral response of the surface, primarily due to the combustion of biomass, changes in soil exposure, and the deposition of charcoal and ash. The magnitude and persistence of these spectral changes depend largely on fire intensity, vegetation structure, and post-fire recovery dynamics [14–16].

The spectral region most sensitive to fire effects lies in the near-infrared (NIR) and short-wave infrared (SWIR) ranges, which has led to the widespread use of spectral indices combining these bands to enhance the detection of burned areas [17–23]. Fires typically induce a strong decrease in NIR reflectance, due to the loss of leaf structure and pigments, and a concurrent increase in SWIR reflectance, associated with vegetation desiccation and increased soil exposure [18,24]. Despite their effectiveness, remote sensing methods for burned area detection still face several limitations. Cloud cover, smoke, and atmospheric effects often obscure the surface, reducing data availability and accuracy [25,26]. Topographic shadows and illumination variability introduce further uncertainties, especially in mountainous areas [23,27,28]. Moreover, rapid post-fire vegetation recovery, seasonal changes, and non-fire disturbances, such as ploughing, drought, or deforestation, can produce spectral signatures similar to those of burned areas, complicating classification [29,30]. These challenges highlight the importance of multi-temporal analyses and topographic and atmospheric corrections to improve the reliability of burned area mapping.

Over time, several number of global and regional BA products have been developed based on the spectral detection of fire-induced vegetation scars, providing standardized datasets at varying spatial and temporal resolutions to support both large-scale monitoring and local fire management. Currently available BA products at both global and regional scales, such as MODIS MCD64A1 (500 m), CLMS Global BA v3 (300 m), and FireCCI50 (250 m), provide extensive coverage suitable for large-scale monitoring of fire dynamics. In Europe, regional products like the European Forest Fire Information System (EFFIS) Burnt Area product leverage higher-resolution data from MODIS (250 m) and Sentinel-2 (20 m) to deliver more detailed and near-time mapping, allowing the detection of smaller burned areas and supporting operational fire management [9,31,32].

Despite their broad coverage, global and regional BA products often underestimate the total burned area due to coarse spatial resolution, which limits the detection of small fires, and the intrinsic characteristics of Mediterranean fires, such as rapid progression, low-biomass vegetation, and fast post-fire recovery [33,34]. For these reasons, given the frequency and spatial variability of fires in Sardinia, the development of a regional-scale monitoring system based on Sentinel-2 data and locally calibrated methods represents a crucial step toward improving the precision and timeliness of burned area information, effectively complementing national and European monitoring frameworks.

In this study, we present an operational approach for BA mapping in Sardinia (Italy), using multi-temporal Sentinel-2 MSI imagery and an MMU (Minimum Mapping Unit) of 1600 m^2. The method builds upon the conceptual framework of the multi-temporal approach proposed by [27], while incorporating local calibration through a Random Forest model and integrating topographic information from a Digital Terrain Model (DTM). The goal is to develop a high-resolution and accurate methodology for BA detection, for annual updates, that outperforms existing global products and provides a reliable tool for environmental monitoring and forest management.

2. Materials and Methods

2.1. Study Area

Sardinia is an Italian island covering approximately 24,090 km^2, making it the second largest island in the western Mediterranean after Sicily. The island features a predominantly mountainous interior, with its highest peak, Punta La Marmora in the Gennargentu Range, reaching 1834 m. Coastal areas are generally rocky with some bays and beaches, while alluvial plains, such as the Campidano plain, host the main agricultural lands. The landscape is highly heterogeneous, with steep slopes and abrupt landforms interspersed with gentler areas. The dominant land covers are natural surfaces, including forests, grasslands, and sclerophyllous vegetation, while agricultural areas account for approximately 10% of the island's surface (Figure 2).

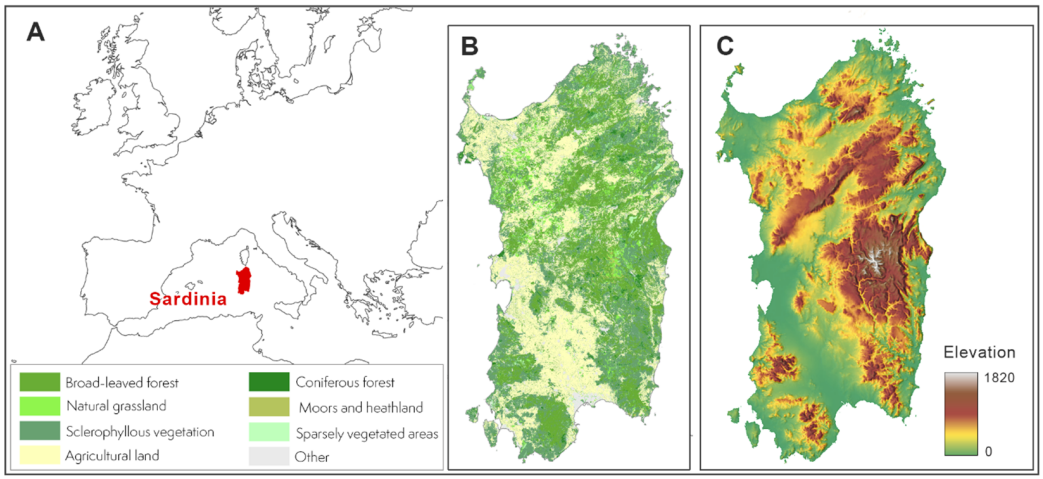

Figure 2. Geographical and biophysical context of Sardinia (Italy): (**A**) Geographical location of Sardinia in the context of the Euro-Mediterranean region. (**B**) Natural land cover map of Sardinia (Sardinia Land Cover Map-2020, see Section 2.2.4), categorized into key vegetation types including forests (Broad-leaved, Coniferous), natural formations (Natural grassland, Sclerophyllous vegetation, Moors and heathland), and Sparsely vegetated areas. (**C**) Digital Terrain Model (Sardinia DTM 10 m, see Section 2.2.3) showing the topography of Sardinia, with colors indicating altitude (m a.s.l.), ranging from sea level (0) to the highest elevations (1820 m).

The island is an area characterized by a high risk of wildfires, an endemic threat that shapes its landscape and deeply impacts its ecology and human communities. Situated in a climatically vulnerable region, with a Mediterranean climate, characterized by wet winters and dry summers, with high temperatures often exceeding 35 °C, the Sardinian region presents a complex interaction of geographical, topographical, and vegetation factors that make it particularly susceptible to large-scale fire events, due to its extensive cover of Mediterranean scrub, grasslands, and forests, coupled with typical summer conditions of drought, strong winds and high temperatures. For these reasons, the wildfire season in Sardinia spans from early June to late September, with peak fire activity occurring from mid-July to early August [35,36].

2.2. Data

This study integrates multiple datasets to develop, train, and validate a BA detection approach for Sardinia. The training and reference datasets were generated through the combined use of Sentinel-2 MSI imagery and the official (CFVA) BA inventory, ensuring accurate spatial delineation of fire-affected zones. The classification was performed using Sentinel-2 time series and the DTM of Sardinia, which provided topographic information to account for illumination and slope effects on spectral responses. The Sardinia Land

Cover Map (2020) was further employed to restrict the analysis to natural land cover classes, excluding urban and agricultural areas. Finally, for a comparative assessment, the proposed method was compared against all currently available BA products covering the study area for the 2024 fire season. While global datasets (MODIS MCD64A1 and CLMS Global BA v3) were included to provide a broad thematic benchmark, the primary comparative analysis focuses on the EFFIS Burnt Area product, as it represents the current operational standard for large-scale fire monitoring in Europe and offers a more comparable regional perspective.

2.2.1. Sentinel-2 MSI Images

The Sentinel-2 mission, part of the Copernicus Programme coordinated by the European Space Agency (ESA), provides freely accessible multispectral imagery designed to support terrestrial and environmental monitoring at both global and regional scales. The constellation consists of two satellites, Sentinel-2A and Sentinel-2B, launched in June 2015 and March 2017, respectively, operating in a sun-synchronous orbit to ensure high revisit frequency and temporal consistency. Each satellite carries a MultiSpectral Instrument (MSI) that acquires 13 spectral bands spanning the visible, near-infrared (NIR), and shortwave infrared (SWIR) regions, with spatial resolutions of 10, 20, and 60 m depending on the band. These data enable applications such as land-cover classification, vegetation health assessment, and water quality monitoring. Sentinel-2 data are available as Level-1C (Top-of-Atmosphere reflectance) and Level-2A (Surface Reflectance) products, the latter obtained through atmospheric correction applied using the Sen2Cor processor [37,38]. The topographic correction applied in Level-2A products can sometimes overcompensate shaded slopes, producing artefacts that may be misinterpreted as BA [27,39,40].

Preliminary tests (Figure 3) comparing Level-1C (TOA) and Level-2A (BOA) products across the study area indicated that while radiometric differences were negligible in lowland and flat regions, significant discrepancies emerged in mountainous areas. In rugged terrains the Sen2Cor topographic correction often introduces significant overcorrection artefacts on steep, shaded slopes. These artefacts resulted in a higher noise-to-signal ratio compared to Level-1C (L1C) data, potentially leading to false positives in burned area detection. Considering that the study region exhibits a large variation in terrain slopes and elevations, Level-1C TOA reflectance data were selected to preserve the original radiometric properties.

In this study we used the following: (i) for the training dataset, a total of 1579 Sentinel-2 MSI images, level 1C covering the year of 2020 and the first six months of 2021 were selected, and (ii) for the BA classification, a total of 1745 Sentinel-2 MSI images, level 1C covering the year of 2024 and the first six months of 2025 were selected. These additional images acquired outside of the temporal window of the years under investigation were included to assess the post-fire conditions of fire events potentially occurred towards the end of 2020 and 2024, which will not be used for the detection of BAs. The Sentinel-2 MSI images of both 2020 and 2024 datasets have been pre-processed through cloud masking to exclude cloudy pixels, using Sentinel Hub's Cloud Probability map, the Scene Classification Layer (SCL) in the Level-2A product, applying a probability threshold of 30%. This not too restrictive threshold might appear unsuitable for our analysis, which is highly influenced by cloud-related disturbances. However, employing a lower probability threshold could result in masking dark areas associated with fire events, as they may be misclassified as cloud shadows [41]. The spectral indices were computed from the pre-processed dataset based on the formulas provided in Table 1.

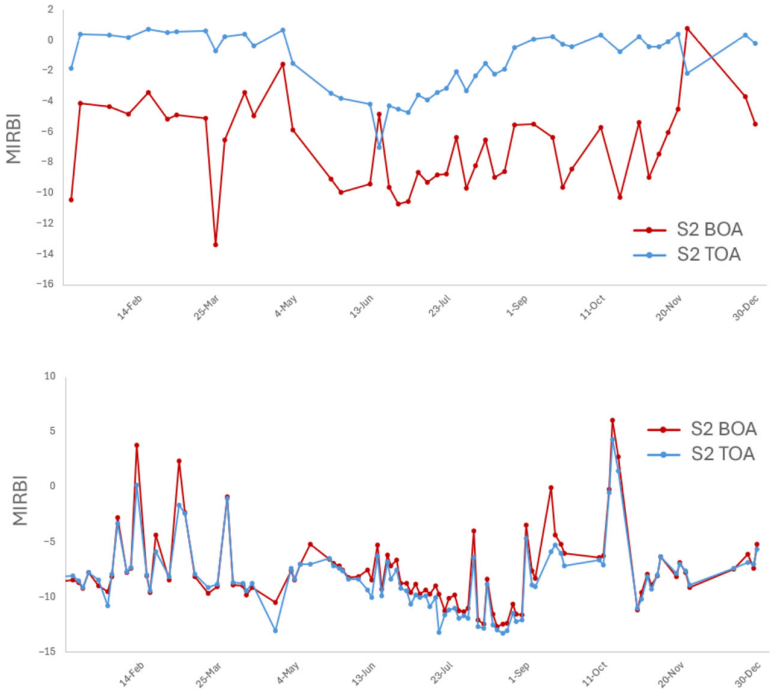

Figure 3. Comparison of Top-of-Atmosphere (TOA, Level-1C) and Bottom-of-Atmosphere (BOA, Level-2A) 2020 MIRBI time series across different topographic settings. In mountainous areas (**A**), the TOA signal exhibits higher stability and significantly less noise compared to the BOA signal, which is affected by topographic overcorrection artefacts on steep, shaded slopes. Conversely, in lowland areas (**B**), the two signals show negligible differences, with TOA and BOA reflectance values remaining closely aligned.

Table 1. Spectral indices analyzed in this study with relative formulas and Sentinel-2 MSI bands used.

Spectral Index	Formula	Sentinel-2 MSI Bands
NDVI	$\frac{NIR-RED}{NIR+RED}$	NIR (B8) RED (B4)
NBR	$\frac{NIR-SWIR_2}{NIR+SWIR_2}$	NIR (B8) $SWIR_2$ (B12)
MIRBI	$10 \times SWIR_2 - 9.8 \times SWIR_1 + 2$	$SWIR_1$ (B11) $SWIR_2$ (B12)
NBR+	$\frac{SWIR_2-RE_4-GREEN-BLUE}{SWIR_2+RE_4+GREEN+BLUE}$	Red Edge 4 (RE_4) $SWIR_1$ (B11) $SWIR_2$ (B12)
BAIS2	$\left[1-\sqrt{\frac{RE_2 \times RE_3 \times RE_4}{RED}}\right] \times \left(\frac{SWIR_2-RE_4}{\sqrt{SWIR_2+RE_4}+1}\right)$	RED (B4) RE_2—Red Edge 2 (B6) RE_3—Red Edge 3 (B7) RE_4—Red Edge 4 (B8A) $SWIR_2$ (B12)

2.2.2. GPS Field Measurements of Burned Areas (CFVA 2020 and CFVA 2024)

The "Catasto dei Focolai e dei Vegetali percorsi dal Fuoco" (CFVA) is an official national inventory maintained by the municipalities of Sardinia, documenting forested and pasture areas affected by wildfires. This registry was established to enforce specific legal restrictions aimed at protecting the environment and facilitating the recovery of fire-impacted areas. According to the Italian Forest Service, the CFVA is updated annually by municipalities, as mandated by Article 10 of Law No. 353/2000. This law requires

municipalities to delineate and report areas affected by wildfires within 90 days of the fire's extinction. The updated data is then transmitted to national authorities and the Ministry of the Environment. The CFVA BAs are mapped through GPS-assisted ground surveys, high-resolution satellite images, and aerial drone imagery to ensure accurate georeferencing and detailed delineation [42].

This dataset serves multiple purposes, including prevention of illegal development, environmental protection and forest management support, providing essential information for planning and implementing forest management and wildfire prevention strategies.

2.2.3. The Digital Terrain Model (DTM) of Sardinia

The DTM of Sardinia represents the regional topography on a 10 m regular grid and was derived from the contour lines and spot elevation layers of the 10 K Geotopographic Database. Data processing was conducted in ArcGIS using the 3D Analyst and Spatial Analyst extensions, including verification of source layers, creation of TINs, conversion to GRID format, mosaicking, assignment of NoData values to water bodies, and reprojection from WGS84 UTM32 to Roma 40 Gauss-Boaga. The resulting DTM provides high-resolution topographic information suitable for hydrological modeling, terrain analysis, wildfire risk assessment, and forest management [43].

2.2.4. Land Cover Data

The Sardinia Land Cover Map (2020) was developed in the framework of the project 'Sardinia Land Cover Mapping', promoted by Regione Autonoma della Sardegna and University of Cagliari. This Land Cover Map was produced as a dynamic, high-resolution dataset integrating Sentinel-2 MSI data and Sentinel-1 C-band SAR Level-1 GRD product with a variety of ancillary data, including orthophotos, topographic databases, OpenStreetMap, and previous regional land use maps. The legend is based on a modified CORINE classification, comprising 34 classes, primarily at level 3, with some level 4. The map was produced through a semi-automatic workflow combining pixel-based classification in Google Earth Engine, object-oriented segmentation, and visual inspection, allowing continuous refinement of class definitions and integration of new data [44,45].

2.2.5. EFFIS Burnt Area Product

The European Forest Fire Information System (EFFIS) Burnt Area product provides near real-time mapping of fire-affected regions across Europe. It integrates satellite imagery from MODIS (250 m) and Sentinel-2 (20 m) to detect and delineate burnt areas, updated up to twice daily. Active fires are identified through thermal anomaly detection, and burnt areas are delineated based on the spatial–temporal evolution of these signals. The minimum mapping unit is approximately 30 ha for MODIS-based estimates, with Sentinel-2 enabling detection of smaller areas. The dataset is openly accessible through the Copernicus EFFIS portal and covers continental Europe and surrounding regions, enabling large-scale monitoring of wildfire extent and impacts. For this study, the total burned areas mapped by EFFIS for 2024 were used as a reference for comparison with the burned area product derived in this work [9].

2.2.6. CLMS Global BA v3

The Copernicus Land Monitoring Service (CLMS) Burnt Area product provides spatially explicit mapping of fire-affected regions at a 300 m resolution, updated on a monthly basis from 2019 onward. The product is derived from Sentinel-3 imagery through the analysis of multi-temporal spectral changes, capturing alterations in vegetation and surface reflectance caused by fire events. Burnt areas are delineated using automated algorithms that compare pre- and post-fire conditions, enabling consistent detection of fire-impacted

surfaces over large regions. Data are provided in netCDF format and are openly accessible via the Copernicus Land Monitoring Service portal [32]. The total burned areas of 2024 mapped in CLMS global BA v3 were used solely for comparative purposes with the burned area product derived in this work.

2.2.7. MODIS Burned Area Monthly Global 500 m (MCD64A)

The MODIS Burned Area Monthly Global (MCD64A1) product is a global, monthly, 500 m gridded dataset that provides per-pixel burned area information derived from MODIS Surface Reflectance and Active Fire data. This product is generated using a hybrid classification approach that relies on dynamic thresholding of a burn-sensitive Vegetation Index (VI) and incorporates 1 km active fire observations. Available as a monthly tiled product, the MCD64A1 dataset has a fine 500 m spatial resolution, with its primary data layer mapping the precise Burn Date (recorded as the ordinal day of the year) for each detected burned pixel [31]. For this study, the MCD64A1 Burned Area product for 2024 was utilized for comparative analysis with the burned area product developed in this work.

2.3. Methods

The proposed methodology was designed to produce operational, high-resolution mapping of burned areas (BAs) in Sardinia using Sentinel-2 MSI imagery and ancillary geospatial datasets. The workflow integrates multi-temporal spectral analysis, machine learning classification, and spatial post-processing to detect, delineate, and validate fire-affected areas with improved accuracy over existing global products. It consists of five main phases: (i) construction of training and reference burned polygons, (ii) evaluation and selection of spectral indices, (iii) detection and delineation of burned areas through a multi-temporal approach, (iv) refinement of results using a Random Forest (RF) model, and (v) final post-processing and validation. Image selection, preprocessing, and visual interpretation of Sentinel-2 MSI data, as well as the detection and delineation of BAs using the multi-temporal approach, were performed within the Google Earth Engine cloud platform. The evaluation of spectral indices performance and the refinement of the BAs detection results using the RF model were carried out in the R environment (version 4.3). The final post-processing and validation phases were conducted using GIS software, including ArcGIS Pro (version 3.3) and QGIS (version 3.34).

2.3.1. Training and Reference Polygons

Both the training and validation datasets consist of polygons representing BAs mapped in Sardinia, for the years 2020 and 2024, respectively. The temporal gap between 2020 (training) and 2024 (validation) was strategically selected to evaluate the model across diverse climatic scenarios, as 2024 marked the culmination of a steady warming trend and record-breaking spring droughts in Sardinia [46].

The 2020 dataset was used for evaluation and selection of spectral indices and training the BAs mapping algorithm, while the 2024 dataset was constructed following the same protocol and reserved as an independent validation set. The use of a different year for validation not only ensured testing on previously unseen data but also allowed us to assess the robustness and transferability of the methodology across years, thus evaluating its potential as a long-term monitoring tool. BA polygons were generated by integrating GPS field measurements of burned areas (CFVA 2020 and CFVA 2024) with a visual interpretation of Sentinel-2 imagery. The photo-interpretation process was carried out using the Google Earth Engine platform (GEE). To enhance the visual identification and delineation of fire-affected zones, Normalized Burn Ratio (NBR) index maps were applied.

Sentinel-2 images from dates preceding and following the fire events were used to validate and refine the GPS-derived polygons. In a subsequent phase, NBR maps generated

from cloud-free Sentinel-2 imagery were analyzed to identify additional fire-affected areas not captured by the CFVA datasets. For each BA polygon detected, the day of year (DoY) on which the fire event was first visibly detectable in Sentinel-2 imagery was also recorded, based on the earliest cloud-free observation showing clear burn evidence.

Although the reference dataset was refined through expert visual interpretation of Sentinel-2 imagery, the potential risk of overfitting or circularity is considered limited. The reference polygons primarily rely on official GPS field measurements, while Sentinel-2 was used solely as a support and geometric refinement step, particularly to correct potential spatial inaccuracies in the GPS tracks and to complete marginal areas not fully covered during field surveys. The use of Sentinel-2 ensures consistency with the observational capabilities of the mapping framework, whereas the adoption of very-high-resolution imagery (e.g., SPOT or PlanetScope), although potentially beneficial, is constrained by limited availability and high acquisition costs over large areas and long time.

The resulting training and reference BA polygons were then filtered using the Land Cover map to isolate those affecting natural vegetation, excluding urban areas, agricultural lands, wetlands, and water bodies.

Natural vegetation was defined according to the following Corine Land Cover classes: 'Broad-leaved forest' (311), 'Coniferous forest' (312), 'Natural grasslands' (321), 'Moors and heathland' (322), 'Sclerophyllous vegetation' (323), and 'Sparsely vegetated areas' (333). To ensure consistency and spatial relevance, a minimum area threshold of 1600 m^2 was applied.

2.3.2. Evaluation of Spectral Indices

Several spectral indices sensitive to post-fire spectral response have been developed to map and quantify the severity of BAs [22,23,47].

The most widely used indices include the Burned Area Index (BAI), designed to enhance the spectral characteristics of charcoal and ash [47], the Normalized Burn Ratio (NBR) by contrasting NIR and SWIR reflectance [48], the Mid-Infrared Bi-Spectral Index (MIRBI), which utilizes Mid-Infrared wavelengths [20], the Normalized Difference Vegetation Index (NDVI) [49], the Burned Area Index for Sentinel-2 (BAIS2), specific for Sentinel-2 [22], and the recently proposed Normalized Burn Ratio Plus (NBR+), incorporating blue and green bands to suppress false positives from water and clouds [23].

Selecting the optimal spectral indices to detect burned areas is crucial for achieving accurate, reliable, and timely wildfire assessments. Different spectral indices exploit distinct combinations of satellite bands to highlight post-fire changes in vegetation and soil reflectance, but their effectiveness can vary significantly depending on the sensor characteristics, land cover types, and presence of confounding elements like water bodies or clouds [27]. Furthermore, change detection methods using bi-temporal analyses (comparing pre- and post-fire images), improve reliability in delineating the exact extent and pattern of burned areas and allowing for more nuanced grading of fire severity [16,50–52].

For the reasons outlined above, an analysis was conducted to evaluate the performance of these indices in detecting BAs. The goal of this study was to identify the most effective spectral indices for accurate post-fire mapping and to assess their reliability in various environmental conditions. The spectral indices considered in this analysis were selected based on their widespread use in remote sensing applications for burned area detection, and include NDVI, NBR, MIRBI, BAIS2, NBR+ (Table 1), along with Sentinel-2 VIS bands (B3, B3 and B4), B8 NIR band and SWIR bands (B11 and B12).

In order to evaluate the ability of the selected spectral indices and Sentinel-2 MSI bands to discriminate between burned and unburned surfaces, 5417 random points were sampled within the training polygons, along with 6000 random points distributed across

natural, unburned areas in the Sardinian territory. For each burned point, spectral values were extracted from the first available cloud-free Sentinel-2 image acquired after the fire event, while for unburned points values were taken from summer cloud-free composites, representing the fire season conditions typical of the Sardinian landscape. For each point, spectral index values and band reflectance were then derived, considering both single-date (i.e., the first available cloud-free image after the fire) and dual-date configurations (i.e., the difference between post-fire and pre-fire values). Then, the Separability Index (SI), a widely used metric in burned area mapping [22,27,53], was computed to quantitatively evaluate how effectively each spectral index distinguishes burned from unburned areas. SI is defined as:

$$SI = \frac{|\mu_b - \mu_{nb}|}{\sigma_b^2 - \sigma_{nb}^2}, \quad (1)$$

where μ_b and μ_{nb} are the mean index values for the burned and unburned classes, respectively, and σ_b and σ_{nb} are the corresponding standard deviations [54,55]. The indices with the highest SI values (see Section 3.2, Figure 7a), specifically MIRBI, B8, and NBR (particularly in their dual-date configurations) were identified as the most effective for distinguishing between burned and unburned surfaces.

Based on these findings, a systematic evaluation was conducted using ROC curve analysis [56] to identify the optimal spectral indices, considering only those with an SI > 1.5. Both individual indices and pairwise and triple combinations were tested. For each index or combination, the ROC curve was calculated using burned versus unburned reference samples, and the optimal thresholds were selected by maximizing the Youden Index. The combination with the highest AUC was identified as providing the best discriminative capability. Although several combinations achieved similarly high discriminative performance, the dual-date MIRBI (dMIRBI) consistently provided the highest separability, with minimal improvement from additional indices (see Section 3.2). Furthermore, due to memory and processing constraints inherent to large-scale analyses in the Google Earth Engine (GEE) environment, the dual-date MIRBI (dMIRBI) was preferred as the primary spectral index for threshold-based burned area detection, as it provided the highest AUC value, while ensuring computational efficiency. In parallel, the near-infrared band (B8) was applied as a preliminary spectral constraint to exclude snow-covered areas. Subsequently, B8 and NBR (in both single and dual configurations) were incorporated in a refinement phase to improve the spatial accuracy of BA delineation.

2.3.3. Detection and Delineation of BAs

Although the previous analyses demonstrated a high spectral separability between burned and unburned surfaces, it is important to acknowledge that significant commission errors occur. These errors often arise from spectral confusion with non-fire-related disturbances such as dark soils, agricultural activity, water bodies, terrain or cloud shadows, etc., due to their similar spectral signals [23,27,57].

The integration of multi-temporal approach is fundamental to mitigate these effects and to identify abrupt, fire-driven spectral changes [51,58]. For this reason, each Sentinel-2 image was analyzed using a multi-temporal analysis, which includes the current processing date, the two temporally closest preceding image and the temporally closest subsequent image. This approach allows us to filter out transient disturbances such as cloud cover, cloud shadows, or atmospheric nois, which may temporarily alter spectral response without being linked to any fire-related event. In addition to the short-term analysis, the spectral response is also evaluated over a medium-term (30 days) and long-term (60 days) period following the potential fire event. This extended temporal analysis helps to further validate the detected burned areas by capturing the evolution of vegetation recovery and better

differentiate the fire-related changes from other long-lasting disturbances in the landscape, e.g., land cover changes, prolonged disturbance caused by extended cloud cover periods, terrain shadows, etc. To better control the topographic shadows, the DTM, discussed in Section 2.2.3, and a baseline estimated by computing the 5th percentile value from the temporal series of the MIRBI were used. This approach allowed us to characterize the minimum spectral response expected under persistent shadow conditions, thereby providing a robust reference for distinguishing true post-fire spectral anomalies from terrain-related low reflectance artifacts.

The BAs detection workflow will be explained in detail in the following sections. This includes the extraction of potential burned areas, followed by a refinement phase using Random Forest model to reduce the commission error of the detected areas. Finally, a post-processing step will be applied to precisely delineate the BAs.

Potential BA Detection

The identification of potential BAs for the year 2024 on the island of Sardinia was performed using Google Earth Engine (GEE), which offers access to large remote sensed datasets, including Sentinel-2 imagery, allowing users to process, analyze, and visualize vast amounts of Earth observation data without the need for high-performance local hardware [59]. As previously mentioned, the first step in BA detection is based on multi-temporal analysis of MIRBI. Specifically, the algorithm relies on MIRBI-based metrics, synthetized in Table 2.

Table 2. MIRBI-based metrics used in the detection of potential BAs performed in Google Earth Engine (GEE).

Metric Name	Formula	Description
$MIRBI_i$	-	MIRBI value at the current processing date.
$MIRBI_{p1}$	-	MIRBI value corresponding to the first most recent valid (i.e., non-null) observation preceding the current processing date.
$MIRBI_{p2}$	-	MIRBI value corresponding to the first most recent valid (i.e., non-null) observation preceding $MIRBI_{p1}$, used as control to verify the robustness of $MIRBI_{p1}$ and ensure it does not represent an isolated negative peak.
$MIRBI_n$	-	MIRBI value corresponding to the first most recent valid (i.e., non-null) observation after the current processing date.
$MIRBI_{nm}$	-	Median MIRBI calculated from all images acquired within 30 days after the current processing date, set to null if there are less than two valid observations in the following month, to ensure it remains a representative measure of the medium-term period, especially in cloudy periods.
$MIRBI_{i-p1}$	$MIRBI_i - MIRBI_{p1}$	Difference between the current and preceding MIRBI value.
$MIRBI_{n-p2}$	$MIRBI_n - MIRBI_{p2}$	Difference between the subsequent MIRBI value after the current processing date and $MIRBI_{p2}$.
$MIRBI_{i-p2}$	$MIRBI_i - MIRBI_{p2}$	Difference between the current and $MIRBI_{p2}$.
$MIRBI_{n-i\%}$	$\left\lvert \frac{MIRBI_n - MIRBI_i}{MIRBI_{i-p}} \right\rvert \times 100$	Absolute percentage ratio between the difference observed after the current processing date and the change detected between the current and preceding dates, helps assess the short-term stability of the spectral signal.

Table 2. *Cont.*

Metric Name	Formula	Description
$MIRBI_{nm-i\%}$	$\left\lvert \frac{MIRBI_{nm} - MIRBI_{i}}{MIRBI_{i-p}} \right\rvert \times 100$	Absolute percentage ratio between the difference in the 30-day median MIRBI after the processing date and the current MIRBI, normalized by the difference between current and preceding MIRBI value; used to assess the persistence of the MIRBI signal in the medium term.
Recovery time	Δdays ($MIRBI_n < MIRBI_p + 0.5$)	Number of days elapsed between the current processing date and the first subsequent date when MIRBI drops below a threshold of $MIRBI_p + 0.5$, indicating a return to a spectral magnitude comparable to pre-fire conditions.

These MIRBI-based metrics are combined through a rule-based algorithm to create a preliminary mask of potential burned areas. Each pixel's time series is evaluated against spectral changes before and after the processing date, and the first date that satisfies all conditions is flagged as a potential burned area (BA).

The logic of the algorithm is structured around a set of conditional scenarios, with a pixel being considered a potential burned pixel only if all core preconditions listed in Table 3 are simultaneously satisfied.

Table 3. Core preconditions in the potential BAs detection.

Condition 1	$MIRBI_i > -4.3$
Condition 2	$NIR < 4000$
Condition 3	$MIRBI_{i-p1} > 1.5 \cap MIRBI_{i-p2} > 1.5 \cap MIRBI_{n-p2} > 1.5$
Condition 4	$MIRBI_n > MIRBI_{p1}$
Condition 5	$recoverytime \geq 15$

These conditions are designed to capture the characteristic fire-induced spectral disturbance, an abrupt rise in MIRBI relative to the previous acquisition, while ensuring that the post-event MIRBI remains above the pre-fire level for at least 15 days, thus filtering out both isolated positive spikes caused by transient non-fire disturbances, and negative peaks in the previous images that can lead to false positive (Figure 4). In doing so, the condition strengthens the robustness of burned area detection by confirming that the observed change is consistent with a genuine and persistent fire signal rather than a momentary disturbance. In particular:

1. Condition 1, applied to detect potential burned areas, applies the optimal MIRBI threshold identified through ROC analysis to discriminate burned from unburned surfaces.
2. Condition 2, which is introduced to exclude high-reflectance surfaces such as snow, can produce persistently elevated MIRBI values following abrupt spectral changes similar to those caused by fires, but typically exhibit much higher albedo and NIR reflectance ranges than burned surfaces (typically > 6000). This condition constrains NIR reflectance using a deliberately conservative, empirically defined threshold, set well above the optimal NIR threshold for detecting BA (NIR < 1722.2) derived from ROC analysis (see Appendix A, Table A1). The purpose of this higher threshold is not to detect BAs, but solely to reliably filter out high-albedo phenomena such as snow or clouds.

3. Condition 3 is designed to detect abrupt increase in MIRBI that is indicative of fire event. The threshold of 1.5 was determined through ROC analysis. However, to reduce false detections caused by transient fluctuations or noise, additional temporal restrictions are imposed. Specifically, an increase of at least 1.5 must not only occur between the current and previous observation ($MIRBI_{i-p1}$), but it must also be consistent when compared with the observation preceding $MIRBI_{p1}$ ($MIRBI_{i-p2}$), ensuring that the MIRBI rise is not related to an isolated negative peak at $MIRBI_{p1}$. In addition, the increase of 1.5 must persist in the subsequent observation ($MIRBI_{n-p2}$), confirming that the change is sustained over time.
4. Condition 4 is introduced to confirm that the detected increase is sustained over time, by comparing the first most recent valid observation after the current processing date ($MIRBI_n$) with the first most recent valid observation preceding it ($MIRBI_p$). This additional precaution ensures that the spectral change is consistent with a burned surface rather than a transient fluctuation caused by noise or short-term effects.
5. Condition 5, designed to avoid classifying as burned areas those surfaces where MIRBI, after an initial increase, returns to a value comparable to the pre-event level in less than 15 days. Such rapid recovery is unlikely to represent a true burned surface and is often caused by persistent cloud cover.

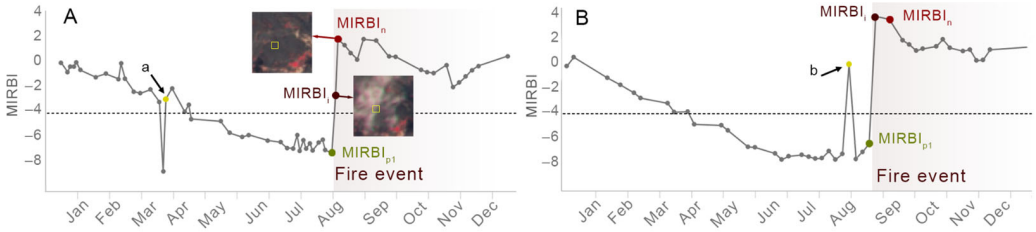

Figure 4. MIRBI time series extracted from different BAs, showing the signal changes after the fire event (red background color in the time series indicates the post-fire period), that illustrates the two main post-fire validation scenarios: (**A**) case where both the short-term ($MIRBI_n$) and the medium-term (30-day median, $MIRBI_{nm}$) values are higher than $MIRBI_i$, due to residual cloud cover affecting the first available image after the fire event ($MIRBI_i$) and artificially lowering the apparent MIRBI signal, thus $MIRBI_n$ is considered more representative of the actual post-fire condition (inset boxes show the Sentinel images corresponding to $MIRBI_i$ and $MIRBI_n$, with a yellow square indicating the exact pixel from which the time series was extracted); (**B**) shows a case where the MIRBI values gradual decline after the fire event, reflecting the typical post-fire recovery trajectory. Both time series display examples where potential noise-related BA candidates (highlighted in yellow) were discarded by the algorithm, as they failed to meet the core conditions, specifically, $MIRBI_{i-p2} > 1.5$ in case (a) and $MIRBI_n > MIRBI_p$ in case (b), allowing for the correct identification of the fire event later in the time series.

Once these conditions are satisfied, two primary temporal scenarios are assessed to validate the fire signal, based on the relationship between the MIRBI value at the current processing date ($MIRBI_i$) and the first subsequent observation ($MIRBI_n$). In the first scenario an increase is observed ($MIRBI_n > MIRBI_i$), thus the stability of the signal is further evaluated by analyzing the 30-day median MIRBI following the event, in order to ensure that the observed increase is not caused by persistent non-fire-related disturbances. In particular, the fire signal is confirmed if:

1. the 30-day median MIRBI ($MIRBI_{nm}$) remains higher than $MIRBI_i$, a behavior which may result from residual atmospheric or surface disturbances affecting the initial detection (e.g., thin clouds, smoke, or shadows) that artificially lower $MIRBI_i$, or from genuine post-fire processes, such as prolonged combustion or soil erosion [1,60], which further intensify the MIRBI response in the following weeks;

2. the 30-day median MIRBI does not decrease by more than 60% relative to the initial MIRBI increase observed after the fire. In the second scenario, a decrease is observed after the event ($MIRBI_n < MIRBI_i$), which represents the most common post-fire behavior; the signal is further assessed to distinguish true fire signals from noise. Specifically, two sub-scenarios are defined based on the percentage drop relative to the initial post-fire increase: if the decrease is too steep ($MIRBI_{n-i\%} > 60\%$), the event is discarded, as it is likely associated with persistent cloud or shadow interference; conversely, if the decrease is moderate ($MIRBI_{n-i\%} < 60\%$) and the 30-day median also remains consistent ($MIRBI_{nm-i\%} < 60\%$), the fire signal is retained. The 60% threshold for the 30-day median MIRBI decrease was selected empirically based on a series of tests where different values (from 10% to 90%, with 10% increments) were evaluated. This analysis showed that for values higher than 60%, the omission rate of burned pixels remains stable. This threshold is therefore a conservative choice, set at the point where true fire signals are maximized, and further increases would only risk including persistent cloud or shadow interference. Importantly, the threshold represents a relative measure of post-fire recovery dynamics: it assesses whether the signal decrease after the initial post-fire increase is unusually steep or moderate. Because it is based on relative changes in the time series rather than absolute MIRBI values, this approach can be reasonably applied to other regions, even with different vegetation phenology or soil backgrounds. Importantly, the threshold represents a relative measure of post-fire recovery dynamics: it assesses whether the signal decrease after the initial post-fire increase is unusually steep (likely due to persistent cloud or shadow interference) or moderate (consistent with true fire recovery). Because it is based on relative changes in the time series rather than absolute MIRBI values, this approach can be reasonably applied to other regions, even with different vegetation phenology or soil backgrounds.

The output of the potential burned area (BA) detection step consists of a set of candidate pixels, each characterized by the timing of the fire event, along with their associated spectral and temporal metrics. In addition to the short-term and medium-term indicators used to identify potential BAs (e.g., MIRBInm, $MIRBI_p1$, etc.), each candidate pixel is also characterized by long-term descriptors, including the 60-day post-fire MIRBI median and the annual 5th percentile baseline, which represent, respectively, the persistence of the fire-induced spectral disturbance and the MIRBI time series baseline.

These potential BAs metrics will be used for the subsequent classification stage, where the final discrimination between true burned areas and false detections is performed.

BA Delineation

The potential burned areas (BAs) from 2020 were used to construct the training dataset for the Random Forest (RF) classifier. Predictor variables included the BA metrics described above (Figure 5) and terrain-derived information (slope, aspect, and elevation). Training samples were collected using a simple random sampling strategy both within the burned perimeters and from the unburned surfaces across the entire study area. This approach was chosen to ensure statistical impartiality and to capture the natural variability of the landscape without subjective selection bias. By distributing points randomly over such a vast and heterogeneous area, the dataset inherently captures the natural proportional distribution of topographic and vegetation characteristics of the region.

The RF model was configured with 1000 decision trees and 4 predictor variables at each split. The trees were grown to maximum depth without pruning, resulting in an average of 3734 terminal nodes per tree. Model performance was evaluated using the out-of-bag (OOB) error, resulting in an overall OOB error rate of 0.66%, revealing high

classification accuracy for both categories: the 'Burned' class achieved a class error of 0.85%, while the 'Non-burned' class showed a lower error rate of 0.49%.

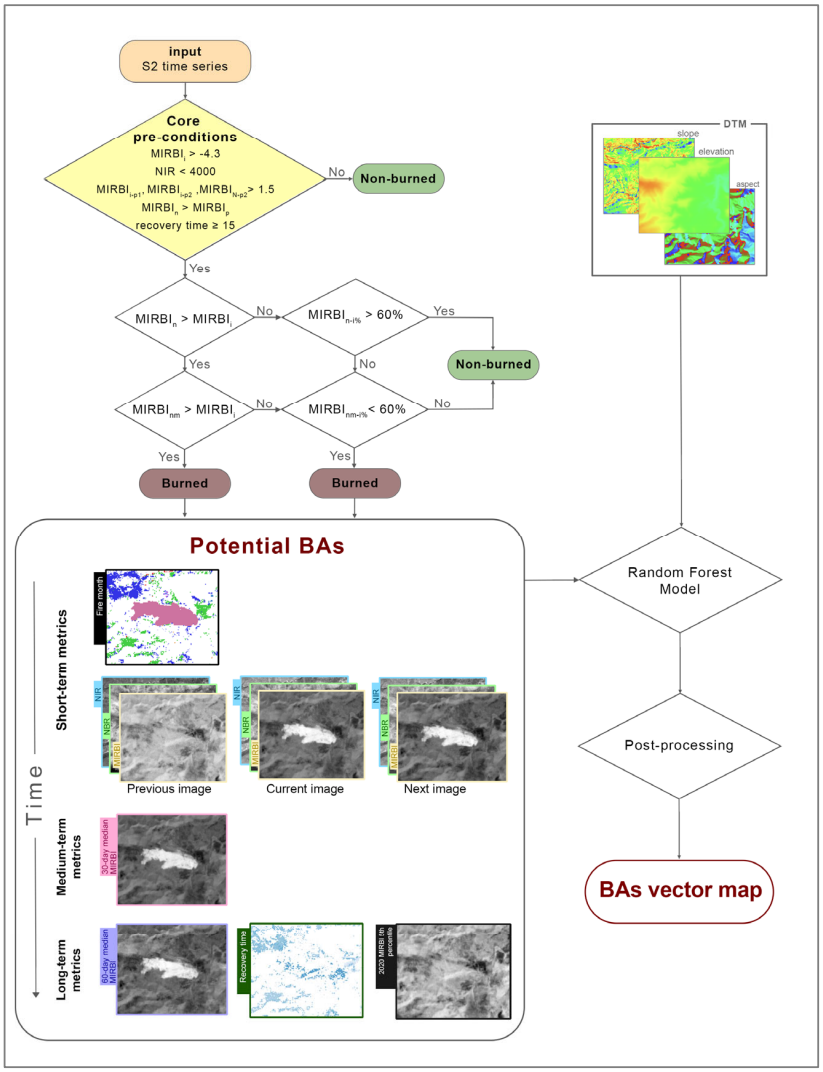

Figure 5. Workflow schema for the BA mapping, including detection and delineation of potential burned areas through a multi-temporal approach using Sentinel-2 MIRBI time series, refinement of results using a Random Forest (RF) model, trained with spectral and topographic parameters and final post-processing.

Once trained, the RF model was applied to delineate potential BAs for the year 2024, allowing the model to better distinguish true fire-affected surfaces from spectrally similar non-fire disturbances, particularly those influenced by terrain-induced illumination effects. Given the complex landscape of Sardinia, terrain shadow-induced disturbances can closely resemble those associated with fire events. In the mountainous areas of Sardinia, an increase in MIRBI values, either abrupt or gradual, depending on terrain slope and aspect, is observed variably from August to April, due to seasonal changes in sunlight exposure conditions. In most cases, however, the MIRBI trend remains relatively stable or increases throughout this period, whereas true post-fire dynamics are typically more variable: after an initial peak, MIRBI values tend to decrease over time (weeks to months, depending on the ecosystem and season) as vegetation regrows and site moisture returns [16,61]. Therefore, both the long-term spectral-based metrics and the terrain-derived variables play a crucial role in this filtering phase. The former help to identify and exclude areas where spectral temporal dynamics are inconsistent with typical post-fire trajectories, while the latter enable

the correction of misclassifications related to topographic effects, particularly those arising from slope- and aspect-dependent illumination conditions. The combined use of these features enhances the reliability of the burned area delineation, minimizing commission errors due to non-fire disturbances in complex mountainous landscapes. Notably, the month of the first post-fire observation, rather than the exact day of year (DoY), was used as a predictor to increase the robustness and generalizability of the classifier across different years.

BA Post-Processing

The raster classified output of the burned area (BA) from the previous step was converted into vector format for further spatial refinement, retaining only those falling within the natural territory of the Land Cover Map (see Section 2.2.4). Small polygons with an area below 1600 m^2 were removed to reduce noise from isolated pixels. In addition, interior gaps within the BA polygons, also smaller than 1600 m^2, were filled to produce contiguous and topologically consistent burned area boundaries.

2.3.4. Validation

Validation of burned area (BA) products is essential to provide users with reliable information on product accuracy and to support the improvement in mapping algorithms [62]. The aim of this study is to provide a temporally consistent and spatially accurate record of fire-affected areas. Accurate validation ensures that the mapped burned areas can be confidently used for long-term monitoring, ecological assessments, and management applications, particularly in a complex and heterogeneous landscape such as Sardinia.

The formal recommendations for BA product validation, such as those provided by the Committee on Earth Observing Satellites' Land Product Validation Subgroup (CEOS LPVS), are formulated for global-scale mapping. These guidelines suggest obtaining reference data with higher spatial resolution than the product under evaluation, covering the same temporal period, and allowing differentiation between new and previous burn scars by using at least two TM acquisitions [63]. Since this study focuses on large scale mapping, some procedures that are typically not feasible for global BA products, such as extensive field surveys or visual interpretation of Sentinel data, can be applied here, providing highly accurate and well-characterized reference data for validation. The reference dataset used for the accuracy assessment, described in Section 3.4, was derived from a combination of GPS field measurements and expert visual interpretation of Sentinel-2 imagery. This dataset was specifically designed to provide a reliable benchmark for the evaluation of the burned area classification [64].

To quantify the agreement between the mapped burned areas and the reference dataset, three complementary metrics were used: the Dice coefficient (DC), the commission error (CE), and the omission error (OE). These metrics are widely adopted for the validation of burned area products derived from remote sensing data [27,65–67]. The equations used to compute the Dice coefficient (DC), commission error (CE), and omission error (OE) are presented in Table 4.

Table 4. Validation metrics and their formulas used in this study to assess the accuracy of the BAs map: Dice coefficient (DC), the commission error (CE), and the omission error (OE).

Validation Metric	Formula
Commission Error (CE)	$CE = \frac{FP}{FP+TP}$
Omission Error (OE)	$OE = \frac{FN}{FN+TP}$
Dice Coefficient (DC)	$DC = \frac{2TP}{FN+FP+2TP}$

3. Results

3.1. Training and Reference Dataset

Burned areas in Sardinia were delineated for the years 2020 and 2024 to construct training and validation polygons, encompassing total burned surfaces of 3264 ha and 4192 ha, respectively. These areas correspond exclusively to natural vegetation classes of Sardinian Land Cover Map (see Section 2.2.4), specifically broad-leaved forest, coniferous forest, natural grasslands, moors and heathland, sclerophyllous vegetation, and sparsely vegetated areas. Comparing these fire statistics to the overall natural area distribution of land cover shows some key discrepancies. Although sclerophyllous vegetation and broad-leaved forest represent the largest natural areas (40% and 44%, respectively) and are, consequently, the most burned in both years, natural grasslands are disproportionately affected. They make up only 10% of the natural area but contributed 23% and 19% of the burned area in 2020 and 2024, indicating a higher relative vulnerability to fire. Conversely, coniferous forest, which accounts for 3% of the natural territories, were barely affected in both years (0.2% and 0.6%). Moors and heathland and sparsely vegetated areas consistently show a low contribution to the burned totals, reflecting their minor percentage in the natural distribution (Figure 6).

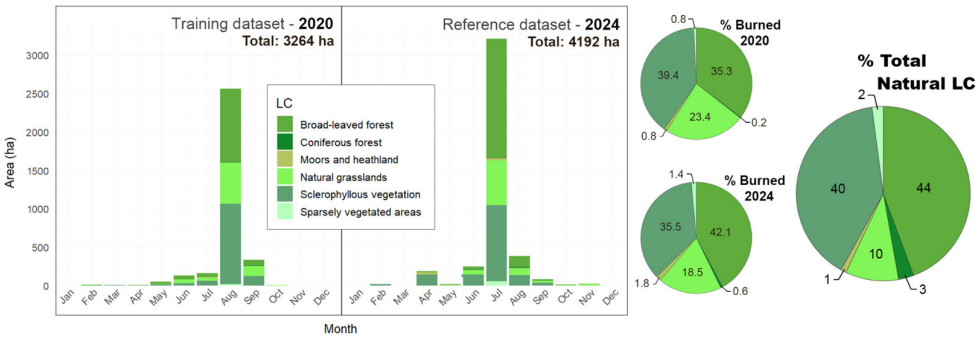

Figure 6. Spatio-Temporal and Land Cover Distribution of Burned Areas (BAs) in the training and reference datasets: on the left, stacked bar charts showing the temporal distribution of burned areas (hectares) per Land Cover (LC) class for the 2020 and 2024 training and reference polygons, respectively, showing the core fire activity in both years being highly concentrated in the peak summer months, primarily July and August, confirming the Mediterranean fire season pattern; on the right, pie charts illustrating the land cover percentage distribution of burned areas in 2020 and 2024, and the percentage land cover distribution in the natural areas of Sardinia island, effectively illustrate that the Land Cover (LC) classes most affected by fire events are indeed those that are most abundant in the regional territory. However, natural grasslands are disproportionately impacted; they represent only 10% of the total natural LC but contribute substantially more to the total BA (23% in 2020 and 19% in 2024), underscoring their high susceptibility to fire, irrespective of their lower abundance.

A comparison between the two fire years, 2020 and 2024, reveals both temporal and spatial shifts in the distribution of burned areas. Regarding the temporal distribution, both years confirm that most fire events occurred during the height of summer, specifically concentrated in July and August. In 2020, the peak of fire season occurred in August, which registered the largest total area burned. The 2024 fire season was highly acute, showing a similar pattern to 2020, with July being the dominant month for fire activity. While the 2020 fire season started in May and extended significantly into June, the fire events in 2024 started earlier, with noticeable activity in April, primarily affecting sclerophyllous vegetation. By 2024, the total burned area increased, and the dominant classes changed slightly: while sclerophyllous vegetation remained highly impacted (35%), broad-leaved forest overtook it as the most affected land cover at 42%. Notably, natural grasslands saw a decrease in their contribution to the burned area (19%), while coniferous forests

experienced a slight increase (0.6%). In both years, sclerophyllous vegetation was the major contributor to the initial summer fires (June–July), but broad-leaved forest appears to be the primary class affected by largest single-event burns observed during the peak of July.

3.2. Evaluation of Spectral Indices

The Separability Index (SI) analysis provided quantitative evidence of the relative effectiveness of the tested spectral indices and Sentinel-2 MSI bands in discriminating between burned and unburned surfaces (Figure 7a). As mentioned in Section 2.3.2, among all indices, the MIRBI, NBR, and B8 (NIR) bands exhibited the highest separability values, particularly when using the dual-date configuration, which integrates pre- and post-fire spectral information (Figure 7b). In particular, the dual-date MIRBI (dMIRBI) achieved the highest separability value (SI = 2.39), indicating a strong ability to discriminate between burned and unburned surfaces. This performance reflects the high sensitivity of MIRBI to post-fire changes in the mid-infrared region, where combustion residues and soil exposure produce marked spectral contrasts [20,21,68,69]. The B8 (NIR) band and the dual-date NBR (dNBR) also exhibited high separability values (SI = 2.06 and 1.84, respectively), confirming their effectiveness in capturing vegetation loss and alterations in canopy structure following fire events [70–72]. Conversely, indices such as dNDVI, dNBR+, and dBAIS2 showed moderate discrimination capacity (SI ≈ 1.5–0.9), while single-date spectral bands in the visible region (B2–B4) presented limited separability (SI < 0.5), as expected due to their lower sensitivity to fire-induced spectral changes [72].

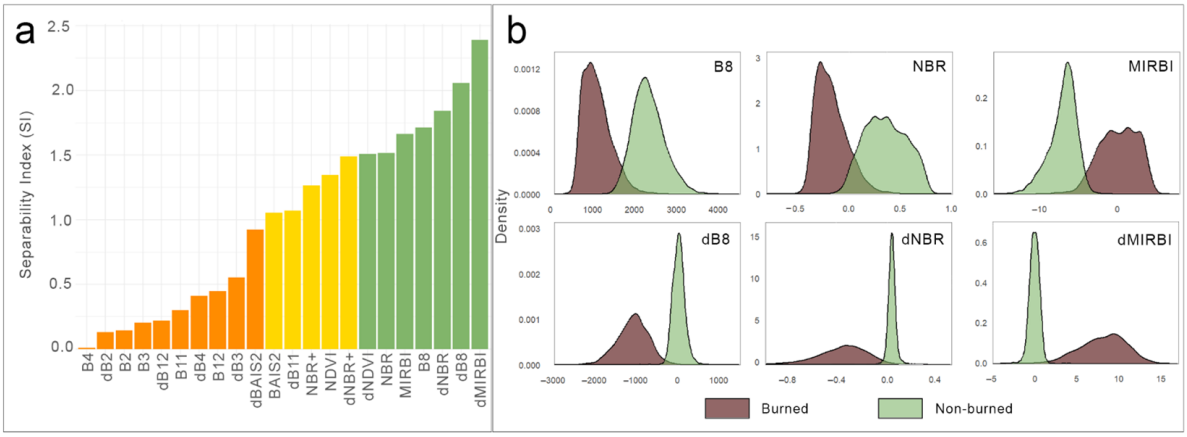

Figure 7. Separability analysis of spectral bands and indices for BA detection. On the left, bar chart showing the Separability Index (SI) of various individual Sentinel-2 bands and spectral indices, with colors indicating SI ranges: orange for SI < 1, yellow for 1 ≤ SI ≤ 1.5, and green for SI > 1.5, with higher values representing better separability (**a**). The analysis confirms the superior performance of the Delta (d-), with dMIRBI and dNBR demonstrating the highest separability; individual bands in the Visible (VIS) spectrum (B2, B3, B4), along with their difference counterparts (dB2, dB3, dB4), exhibit low separability (SI < 0.55), particularly the B4 band which has near-zero separability (SI = 0.008). On the right, density distributions of the best spectral bands and indices for burned and non-burned area discrimination, showing the dual-date indices having a marked improvement in separability (**b**).

Based on the Separability Index analysis, only MIRBI, dMIRBI, B8, dB8 and dNBR exhibited SI values greater than 1.5 and were therefore retained for further evaluation. For these variables, ROC curve analysis (Figure 8) was performed considering individual indices as well as pairwise and triple combinations.

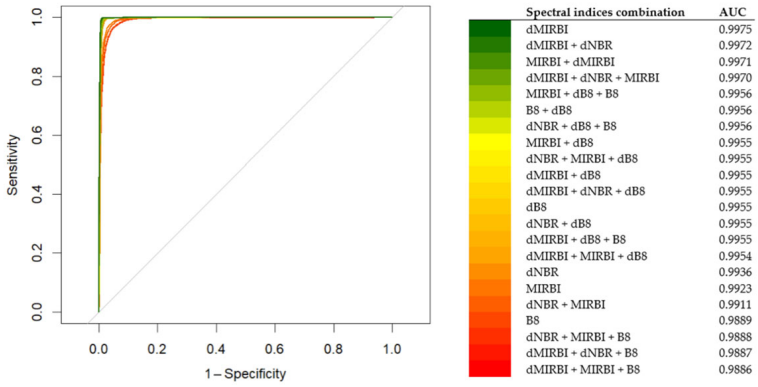

Figure 8. Receiver Operating Characteristic (ROC) curves comparison for single, pairwise, and triplet combinations of B8, MIRBI and NBR in single and dual configuration. The plot illustrates the classification performance (burned vs. unburned) using a color gradient from red (lowest AUC) to dark green (highest AUC). The grey diagonal line represents a random classifier (no discrimination), for reference.

The ROC results indicate that dMIRBI achieved the highest discriminative performance among the individual indices (AUC = 0.997). Pairwise and triple combinations involving dMIRBI yielded similarly high AUC values, but without substantial improvement compared to dMIRBI alone. This confirms that dMIRBI provides near-optimal discrimination between burned and unburned areas, supporting its selection as the primary index for threshold-based burned area detection. Based on these results, MIRBI and dMIRBI were retained for the subsequent burned area detection steps. For both indices, optimal threshold values were derived from the ROC analysis by maximizing the Youden Index. The resulting thresholds were −4.3 for MIRBI and 1.5 for dMIRBI.

These threshold values will be applied in the subsequent classification phase to discriminate burned from unburned surfaces. In contrast, B8 and NBR were integrated into the Random Forest refinement step to improve the spatial precision of burned area boundaries.

3.3. Detection and Delineation of BAs

The burned area detection and delineation workflow produced a set of spatially explicit products representing the progressive refinement of fire-affected surfaces, from the initial potential detections to the final, topologically consistent burned polygons. This section presents the main outcomes derived from the three processing stages described in Section 2.3.3, namely: (i) the identification of potentially burned areas (potential BAs), (ii) their refinement through Random Forest classification (classified BAs), and (iii) the generation of final product, i.e., the BAs vector map, following spatial post-processing (Figure 9).

During the first detection stage, the MIRBI-based rule set identified an extensive number of potential BAs across Sardinia, corresponding to a total of 195,437 ha, equivalent to approximately 8% of the regional territory. Within natural environments only, defined according to the selected CL classes, the detected burned surface amounted to 107,189 ha, representing 7% of the total natural area. A visual inspection of these results revealed that a large portion of false detections was associated with topographic shadow effects, which exhibit spectral behavior similar to post-fire conditions. Furthermore, about 32% of the detected pixels were isolated elements below the minimum mapping unit (MMU) of 1600 m^2. After the refinement step through Random Forest classification, the total burned area estimate decreased substantially to 16,764 ha, corresponding to a 91% reduction relative to the potential BA extent. This reduction primarily reflects the model's ability to filter out non-fire-related disturbances. Nonetheless, approximately 15% of the remaining pixels

were still found below the MMU threshold, indicating residual small-scale noise. Finally, following the post-processing phase, which included polygon filtering and gap-filling restricted only to natural areas, the total final BA amounted to 3885.5 ha. This last step resulted in an additional 11% reduction in the area within natural environments, mainly due to the removal of isolated pixels and the enforcement of spatial consistency rules.

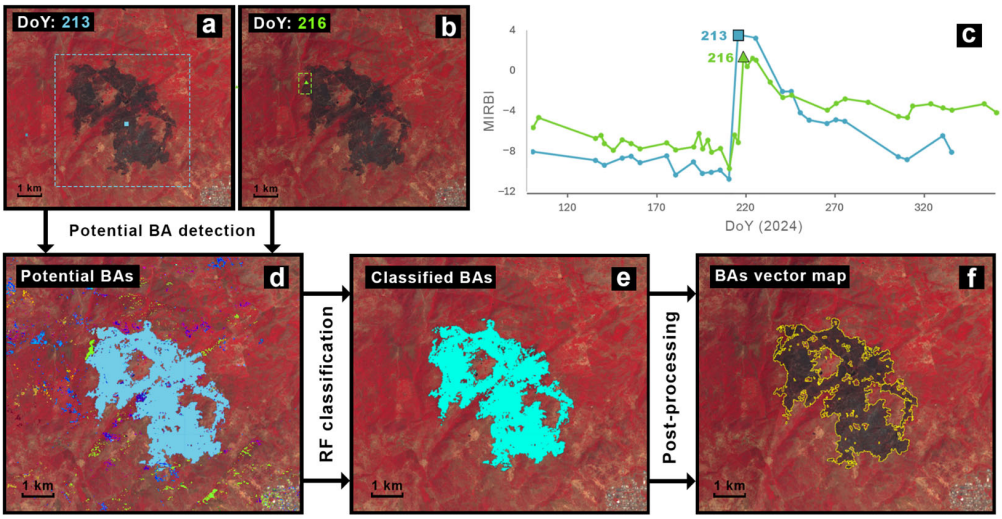

Figure 9. Example of the progressive refinement of burned area (BA) detection through the three processing stages. (**a**,**b**) Post-fire Sentinel-2 false-color composites (NIR–RED–GREEN) acquired immediately after the main fire event (DoY 213, shown in cyan) and three days later (DoY 216, shown in green). The cyan box highlights the main burned area (DoY 213), while the green box indicates a smaller secondary fire detected in the subsequent acquisition (DoY 216). (**c**) MIRBI time series extracted at representative points within the burned areas shown in ((**a**): square; (**b**): triangle), illustrating the typical temporal evolution of fire-affected surfaces, characterized by an abrupt post-fire increase in MIRBI values followed by a gradual decrease associated with vegetation recovery at variable rates depending on land cover, ecosystem type and seasonal conditions. (**d**–**f**) Spatial evolution of the burned area mapping results: (**d**) potential BAs detected from the MIRBI-based algorithm, color-coded according to the day of year (DoY) of first post-fire detection; (**e**) refined BA classification obtained through Random Forest, where most of the noise and false detections from the previous step were removed; and (**f**) final BA vector map after post-processing, showing improved spatial coherence and gap-filling of interior holes smaller than 1600 m^2.

3.4. Validation

The overall performance of the BA classification demonstrates a high level of accuracy, with a Dice Coefficient (DC) of 91.85%, a Commission Error (CE) of 4.53%, and an Omission Error (OE) of 11.51% (Figure 10). The higher omission rate compared to commission indicates that the classification tends to be more conservative, leading to a slight underestimation of the total burned extent, particularly outside the main fire season, such as during spring and winter. This tendency can be partly attributed to the composition of the training burned polygons, which is dominated by summer fire events; consequently, non-summer burns are less well represented and may be misclassified or filtered out as noise due to their weaker or shorter-lived spectral and temporal signatures compared to typical summer burns, which are usually characterized by a more persistent fire signal. Moreover, the reduced availability of clear-sky satellite acquisitions during these months caused by more frequent cloud cover further increases the likelihood of misclassification, as incomplete temporal information limits the model's ability to correctly identify burned areas.

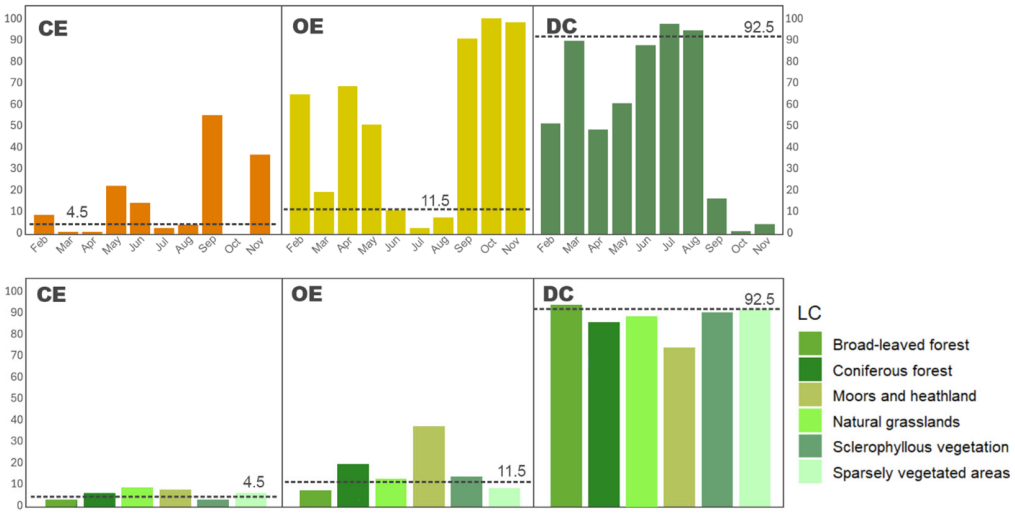

Figure 10. Classification accuracy assessment of Burned Area (BA) by Land Cover (LC) type and monthly variation in classification errors. Overall classification accuracy is indicated by the dashed lines: Commission Error (CE) of 4.5%, Omission Error (OE) of 11.5%, and Dice Coefficient (DC) of 91.8%. Top row: Accuracy by Land Cover type. Bottom row: Monthly distribution of CE and OE. The results show that classification errors are concentrated mainly off-season with OE peaks notably in the non-summer months, and in moors and heathland and coniferous forest LC classes.

While the commission error is mainly observed in small, isolated areas, often associated with noise, fire edges (mixed pixels), or regions that have undergone recent land cover changes, the omission error can be attributed to two main factors. Approximately 54% of the total false negative area results from misclassifications during the potential burned area detection stage, while the remaining 46% arises from the refinement step using the Random Forest model. Omissions during the Potential BA detection stage generally follow the fire season's intensity, with higher errors coinciding with the peak of fire activity in summer (Appendix A, Figure A2). A notable exception occurs in April, where detection omissions remain high relative to the total area burned; this is quantitatively linked to the reduced availability of cloud-free Sentinel-2 acquisitions, which limits the temporal window for identifying BAs. Quantitatively, omissions during the potential BA detection stage are driven in almost equal measure by low post-fire signal intensity (when MIRBI > −4.3 or when the spectral difference between pre- and post-fire acquisitions is less than 1.5) and rapid vegetation recovery (in both immediate and 30-day post-fire window). Additionally, temporal series noise plays a significant role; spectral fluctuations can mimic a premature recovery or a low fire intensity, leading the algorithm to prematurely filter out valid burned pixels as noise or inconsistent data.

Conversely, omissions in the BA delineation stage occur during the off-season (April and September). This reflects a direct dependency on the fire period: since the Random Forest model was primarily trained on summer events, its ability to precisely define perimeters decreases for off-season fires.

In addition, the spatial distribution of classification errors does not reveal systematic patterns across the study area. Both commission and omission errors are relatively uniformly distributed over the entire territory, with no evident clustering related to specific morphological settings.

Regarding the accuracy across land cover types, the highest accuracy is observed for broad-leaved forest, natural grasslands, and sclerophyllous vegetation, with DC values exceeding 89%. These results suggest that the algorithm effectively discriminated burned surfaces in these environments, likely due to their distinct post-fire spectral signatures.

However, natural grasslands also present the highest commission error (9%), indicating a clear tendency to overestimate burned areas in these landscapes. Notably, commission errors larger than 1 ha account for only about 30% of the total commission error area in natural grasslands, indicating that most false positives consist of small, fragmented patches likely related to noise, that can be partly explained by the intrinsic dynamism of grassland ecosystems, where the spectral signal is highly variable and inherently unstable, which may be confused with fire-induced changes. For larger commission errors, misclassifications are often associated with land management practices. In Sardinia, these areas are often used for grazing or occasionally converted for agricultural purposes, where ploughing, especially on dark soils, produced spectral responses similar to those of burned surfaces. Some misclassifications also occurred in zones that have undergone land-use changes in recent years, such as newly built-up areas or sites where agri-photovoltaic installations have been established, further contributing to the observed commission error.

On the other hand, moors and heathland exhibit the lowest accuracy, mainly due to an omission error of 37.3%, the highest among all land cover types. Most of the undetected fires in this class occurred in off-season (see Appendix A, Figure A1 for detailed temporal distribution of errors across different land cover types), when classification performance tends to decrease due to off-season conditions. In addition, the rapid post-fire vegetation recovery typical of these ecosystems shortens the persistence of the fire signal, further complicating detection.

4. Discussion

The results of this study (CE = 4.5%, OE = 11.5%, DC = 91.8%) indicate substantially improved burned-area detection for Sardinia, especially compared to global products. A comparative summary is shown in Table 5.

Table 5. Comparative performance of the proposed classification model and existing Burned Area products based on Commission Error (CE), Omission Error (OE), and Dice Coefficient (DC). While the majority of products rely on satellite-based classification (from coarse MODIS MCD64A1 to high-resolution EFFIS 2024), the CFVA 2024 product is distinct as it is derived from field-based GPS perimeter measurements. The resulting accuracy demonstrates a clear dependency on both spatial resolution and data source. Generally, higher resolutions and the use of ground-based GPS measurements (CFVA 2024) correlate with improved accuracy compared to coarse global products. Crucially, our locally calibrated model outperforms all comparative products, even exceeding the Dice Coefficient of the high-precision CFVA 2024 dataset.

Product	Spatial Resolution	CE (%)	OE (%)	DC (%)
This study	high (MMU = 1600 m^2)	4.5	11.5	91.8
CFVA 2024	high (GPS measurement)	16.9	4.9	88.7
EFFIS 2024	high (20 m)	17.3	22.8	79.9
CLMS global BA v3	medium-coarse (300 m)	31.1	49.0	58.6
MCD64A1	coarse (500 m)	52.0	78.4	29.8

As expected, global burned area products (MODIS MCD64A1 and CLMS BA v3) exhibited lower accuracy levels compared to our model, primarily due to their coarser spatial resolutions which are inherently less suited for capturing the small and fragmented burns.

At higher spatial resolution, the EFFIS 2024 product (20 m, Sentinel-2 refined) performs notably better (DC = 79.9%), demonstrating the benefits of increased spatial detail and improved delineation of burned perimeters. However, its omission (22.8%) and commission (17.3%) errors remain substantial, occurring mainly in natural grasslands and concen-

trated along fire perimeter edges, where mixed or partially burned pixels create spectral ambiguity [73,74]. The high commission error is also driven by the 'rounded' and generalized geometry of EFFIS perimeters; the use of spatial smoothing filters and morphological operators (e.g., buffering or clump-and-sieve) tends to artificially expand perimeters over unburned patches to ensure a continuous shape. Omission errors show a clear dependence on fire size. Approximately 75% of the omitted BAs corresponds to events smaller than 10 ha, with the highest contribution (51%) originating from fires between 1 and 10 ha. In contrast, omission decreases markedly for events larger than 10 ha. This size-dependent behavior indicates that EFFIS is less sensitive to small, fragmented, or low-severity fire events, which are more difficult to detect consistently at continental scale.

In contrast, our locally calibrated classification model shows superior capacity in recognizing and correctly classifying these boundary pixels, largely due to (i) using training data that include examples of mixed-edge pixels, (ii) fine minimum mapping unit, and (iii) more precise delineation thresholds geared to Sardinia's mosaic land cover and fire dynamics. The CFVA 2024 dataset differs substantially from the other products considered, as it is not derived from satellite image classification but from field-based GPS perimeter surveys conducted by the Corpo Forestale e di Vigilanza Ambientale of Sardinia. As such, it represents a highly detailed and regionally focused dataset that captures fire perimeters with great spatial precision and independent ground verification. Despite originating from a completely different data source, our classification still outperforms CFVA by approximately 3% in terms of the Dice Coefficient (91.8% vs. 88.7%). This improvement is mainly attributable to a lower commission error in our model (4.5% vs. 16.9%). The higher commission error observed in the CFVA perimeters likely arises from the manual nature of GPS mapping, in which boundaries are not always drawn precisely on the burned–unburned transition, occasionally including adjacent unburned patches or unburned areas within the fire perimeter (Figure 11).

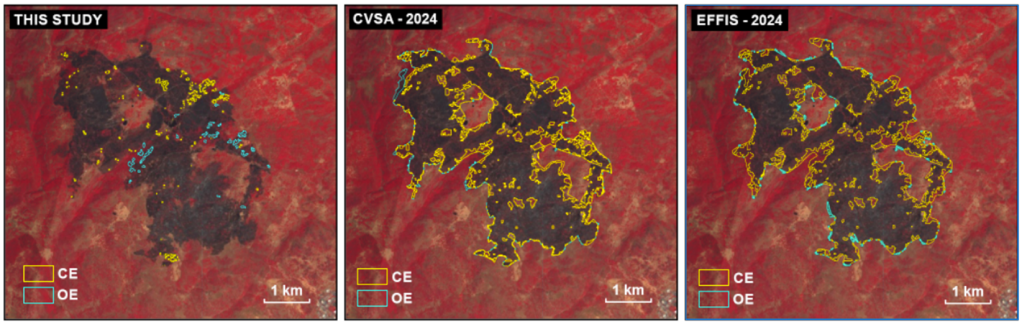

Figure 11. Spatial distribution of Commission Error (CE) and Omission Error (OE) for three high-resolution Burned Area (BA) products overlaid on a Sentinel-2 post-fire false-color composite of a representative fire event. The CE (yellow outlines) and OE (light blue outlines) areas quantify misclassification relative to the validation dataset. Products CFVA 2024 and EFFIS 2024 exhibit substantial CE, mainly associated with the misclassification of unburned internal patches and the inclusion of spectrally ambiguous mixed pixels at the fire perimeter transition zones. Conversely, the model developed in this study achieves a marked reduction in CE and OE, demonstrating superior performance in precise perimeter delineation and robust internal classification, thus confirming the effectiveness of the locally calibrated approach in mitigating spectral ambiguity errors.

However, the proposed classification model, while demonstrating superior accuracy for Sardinian burned-area detection, is not without its limitations. A primary constraint stems from the dependency on cloud-free satellite imagery, a common challenge in optical remote sensing, particularly during the shoulder seasons (spring and autumn) when cloud cover is more prevalent [75,76]. This limitation directly contributes to the omission of some off-season fire events, as previously noted, which are correctly recorded in the CFVA

dataset. It is also worth noting that the lower accuracy values registered in our model are mainly associated with land cover types that are less represented in Sardinia, such as moors and heathland and coniferous forest, which further contributes to their reduced classification performance.

Furthermore, the model exhibits sensitivity to land cover change signals that spectrally mimic burn scars. We observed several commission errors attributable to non-fire related disturbances, including deforestation and logging activities, construction of artificial surfaces, and agricultural disturbances (e.g., ploughing or crop residue burning). Finally, the operational application of this model, hosted on the Google Earth Engine (GEE) platform, is constrained by the GEE user memory limit. For comprehensive or large-area classification tasks, this computational constraint necessitates the subdivision of the classification into various sub-steps. This strategy, while ensuring the successful completion of the analysis, introduces minor operational overhead and requires careful management of the processing workflow.

5. Conclusions

This study aimed to provide a highly accurate and locally calibrated model based on Sentinel-2 MSI data for burned area mapping in Mediterranean environment, specifically for the island of Sardinia, within the broader framework of land cover mapping, environmental monitoring, vegetation dynamics assessment, and landscape change analysis. The model was designed to be robust and temporally consistent, allowing its application across multiple years to produce annual burned area maps.

The workflow consists of four main steps that progressively refine the identification and delineation of burned areas by integrating spectral, temporal, and topographic information within the Google Earth Engine environment. First, Sentinel-2 spectral indices and their thresholds were evaluated, identifying MIRBI, NBR, and NIR as the most effective indicators of BA detection. Second, a multi-temporal MIRBI analysis was applied to detect potential burned areas, exploiting short-, medium-, and long-term temporal windows to capture persistent fire signals and filter out transient disturbances. Third, a Random Forest refinement combined spectral–temporal metrics with topographic variables (slope, aspect, elevation) to improve discrimination from non-fire disturbances such as terrain shadows. Finally, post-processing converted the classified outputs into vector format, applying spatial filtering to remove noise and produce topologically consistent, high-resolution burned area maps suitable for land cover integration.

Validation results (Dice Coefficient = 91.85%) confirm the high accuracy and reliability of the proposed approach, allowing the detection of small and rapid-recovery BAs. Despite its strong performance, the model still presents some limitations mainly related to its dependence on optical imagery, which reduces detection capability under persistent cloud cover and during off-season fires. These events are relatively uncommon and therefore underrepresented in the training dataset, slightly affecting classification accuracy.

Nevertheless, the model proved highly effective in identifying the first post-fire image, achieving an accuracy exceeding 95%. In addition to burned area delineation, the output includes the day of the first post-fire image and all parameters used in classification, such as pre- and post-fire MIRBI, NBR, and NIR values, enabling the estimation of burn severity and post-fire recovery time.

Future improvements could involve the progressive enrichment of the training dataset with new annual samples, particularly for off-season fires, to enhance model generalization and temporal robustness. In this context, future developments may include the adoption of Deep Learning architectures (e.g., CNNs or U-Net), whose ability to model spatial context could naturally mitigate salt-and-pepper effects and reduce reliance on

MMU-based post-processing. With continuous yearly updates, the approach can evolve into a reliable operational tool for systematic burned area mapping, long-term fire regime monitoring, and post-fire ecosystem assessment in Mediterranean environments. Moreover, although the model was specifically calibrated for the Sardinian landscape, its structure and workflow are fully transferable and can be locally re-calibrated to other Mediterranean or fire-prone regions, maintaining comparable levels of accuracy and reliability. Finally, the proposed methodology demonstrated a higher spatial accuracy and consistency compared to field-based GPS surveys, while offering substantial advantages in terms of efficiency, scalability, and operational applicability.

Author Contributions: Conceptualization, C.C. and C.P.; methodology, C.C.; software, D.S.; validation, C.C. and C.P.; formal analysis, C.C.; investigation, F.D. and C.C.; resources, D.S.; data curation, D.S. and F.D.; writing—original draft preparation, C.C.; writing—review and editing, D.S., F.D., M.C., C.P. and M.T.M.; visualization, C.C. and M.C.; supervision, M.T.M.; project administration, M.T.M.; funding acquisition, M.T.M. All authors have read and agreed to the published version of the manuscript.

Funding: This research was funded by the Italian National PhD Program in Earth Observation, funded by the European Union—NextGenerationEU under the Italian National Recovery and Resilience Plan (NRRP), and by a research project named 'Sardinia Land Cover Mapping' (grant number: F23C23000160005), in collaboration with the Regione Autonoma della Sardegna, Servizio Tutela e Gestione delle Risorse Idriche, Vigilanza sui Servizi Idrici e Gestione delle Siccità—Direzione generale Agenzia Regionale del distretto Idrografico della Sardegna.

Data Availability Statement: The datasets presented in this article are not readily available because the data are part of an ongoing study. Requests to access the datasets should be directed to https://www.sardegnageoportale.it/.

Acknowledgments: The authors acknowledge the support of the Regione Autonoma della Sardegna for the collaboration project and of the Italian National PhD Program in Earth Observation for providing the research framework and academic support. The authors also thank all colleagues and institutions that contributed to the study.

Conflicts of Interest: The authors declare no conflicts of interest. The funders had no role in the design of the study; in the collection, analyses, or interpretation of data; in the writing of the manuscript; or in the decision to publish the results.

Appendix A

Table A1. ROC analysis result and optimal thresholds selected by maximizing the Youden Index.

Variable	Threshold	AUC
B2	910.75	0.6208963
B3	936.25	0.6037115
B4	636.75	0.5531063
B8	1722.25	0.988931
B11	1973.25	0.6488905
B12	1194.75	0.7599629
NBR	0.0348599	0.981869
MIRBI	−4.3373499	0.9922898
NDVI	0.2623452	0.9648889
NBR+	−0.4602851	0.9621721

Table A1. *Cont.*

Variable	Threshold	AUC
BAIS2	0.2101454	0.9881262
dB2	−94.75	0.6022082
dB3	−107.75	0.7974249
dB4	−142.75	0.7008126
dB8	−308.75	0.9955223
dB11	−238.75	0.9246589
dB12	135.75	0.6065659
dNBR	−0.0751243	0.9936156
dMIRBI	1.5934005	0.9974516
dNDVI	−0.0340062	0.9795337
dNBR+	0.0479007	0.9784764
dBAIS2	−0.1729811	0.9876758

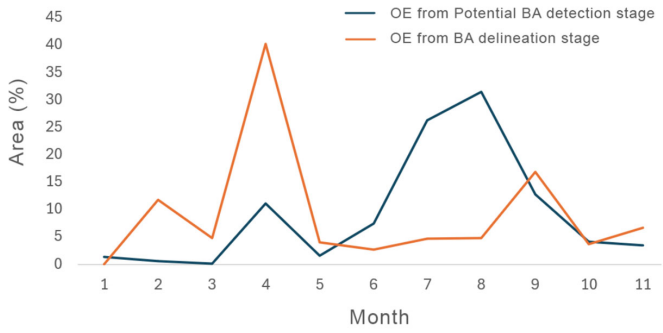

Figure A1. Temporal distribution of omission areas across the validation period. The graph illustrates the percentage of burned area omitted during the two main phases of the algorithm: Potential BA detection in GEE (blue line) and BA delineation through RF model (orange line).

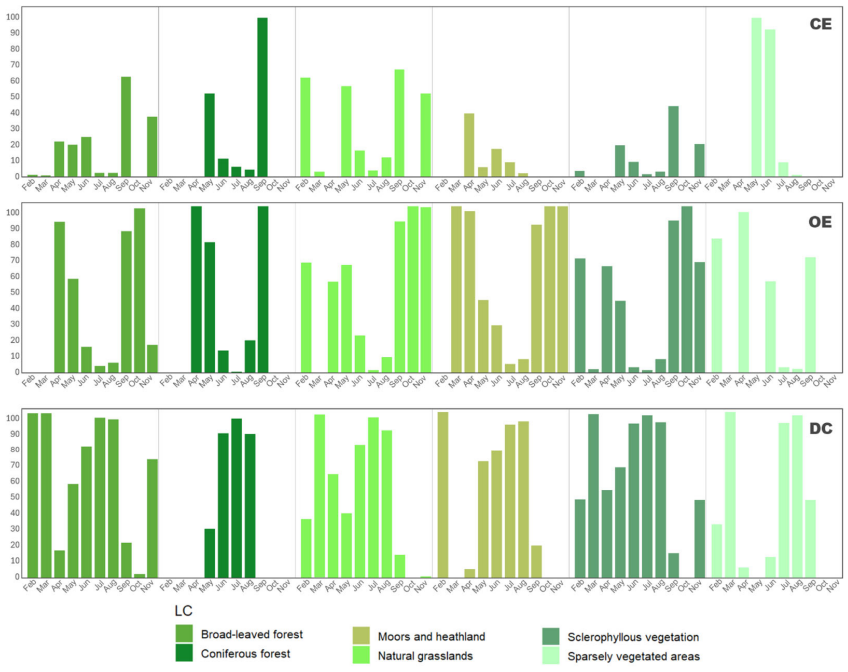

Figure A2. Detailed classification accuracy assessment of Burned Area (BA) by Land Cover (LC) type and monthly variation in classification errors.

References

1. Pala, C.; Melis, M.T.; Pioli, L.; Sarro, R.; Loddo, S.; Cinus, S.; Brunetti, M.T. Sediment generation through thermal spalling during the 2021 montiferru planargia wildfire and its contribution to postfire debris flows. *Sci. Rep.* **2025**, *15*, 30918. [CrossRef]
2. Bowman, D.M.J.S.; Kolden, C.A.; Abatzoglou, J.T.; Johnston, F.H.; van der Werf, G.R.; Flannigan, M. Vegetation fires in the Anthropocene. *Nat. Rev. Earth Environ.* **2020**, *1*, 500–515. [CrossRef]
3. Jones, M.W.; Abatzoglou, J.T.; Veraverbeke, S.; Andela, N.; Lasslop, G.; Forkel, M.; Smith, A.J.P.; Burton, C.; Betts, R.A.; van der Werf, G.R.; et al. Global and Regional Trends and Drivers of Fire Under Climate Change. *Rev. Geophys.* **2022**, *60*, e2020RG000726. [CrossRef]
4. Kelley, D.I.; Burton, C.; Di Giuseppe, F.; Jones, M.W.; Barbosa, M.L.F.; Brambleby, E.; McNorton, J.R.; Liu, Z.; Bradley, A.S.I.; Blackford, K.; et al. State of Wildfires 2024–2025. *Earth Syst. Sci. Data* **2025**, *17*, 5377–5488. [CrossRef]
5. Cunningham, C.X.; Abatzoglou, J.T.; Ellis, T.M.; Williamson, G.J.; Bowman, D.M.J.S. Wildfires will intensify in the wildland-urban interface under near-term warming. *Commun. Earth Environ.* **2025**, *6*, 542. [CrossRef]
6. Salis, M.; Arca, B.; Alcasena, F.; Arianoutsou, M.; Bacciu, V.; Duce, P.; Duguy, B.; Koutsias, N.; Mallinis, G.; Mitsopoulos, I.; et al. Predicting wildfire spread and behaviour in Mediterranean landscapes. *Int. J. Wildland Fire* **2016**, *25*, 1015–1032. [CrossRef]
7. Viedma, O.; Moity, N.; Moreno, J.M. Changes in landscape fire-hazard during the second half of the 20th century: Agriculture abandonment and the changing role of driving factors. *Agric. Ecosyst. Environ.* **2015**, *207*, 126–140. [CrossRef]
8. Moreira, F.; Ascoli, D.; Safford, H.; Adams, M.A.; Moreno, J.M.; Pereira, J.C.; Catry, F.X.; Armesto, J.; Bond, W.J.; González, M.E.; et al. Wildfire management in Mediterranean-type regions: Paradigm change needed. *Environ. Res. Lett.* **2020**, *15*, 011001. [CrossRef]
9. San-Miguel-Ayanz, J.; Durrant, T.; Boca, R.; Maianti, P.; Liberta, G.; Oom, D.; Branco, A.; de Rigo, D.; Suarez Moreno, M.; Ferrari, D.; et al. *Advance Report on Forest Fires in Europe, Middle East and North Africa 2024*; Publications Office of the European Union: Luxembourg, 2025.
10. Hitchcock, H.C.; Hoffer, R.M. Mapping a recent forest fire with ERTS-1 MSS data. In Proceedings of the Remote Sensing of Earth Resources, Volume 3—Third Conference on Earth Resources Observation and Information Analysis System, Tullahoma, TN, USA, 25–27 March 1974; pp. 449–461.
11. French, N.H.F.; Kasischke, E.S.; Hall, R.J.; Murphy, K.A.; Verbyla, D.L.; Hoy, E.E.; Allen, J.L. Using Landsat data to assess fire and burn severity in the North American boreal forest region: An overview and summary of results. *Int. J. Wildland Fire* **2008**, *17*, 432–443. [CrossRef]
12. Chuvieco, E.; Mouillot, F.; van der Werf, G.R.; San Miguel, J.; Tanase, M.; Koutsias, N.; García, M.; Yebra, M.; Padilla, M.; Gitas, I.; et al. Historical background and current developments for mapping burned area from satellite Earth observation. *Remote Sens. Environ.* **2019**, *225*, 45–64. [CrossRef]
13. Nelson, D.M.; He, Y.; Moore, G.W.K. Trends and applications in wildfire burned area mapping: Remote sensing data, cloud geoprocessing platforms, and emerging algorithms. *Geomatica* **2024**, *76*, 100008. [CrossRef]
14. Chuvieco, E.; Lizundia-Loiola, J.; Pettinari, M.L.; Ramo, R.; Padilla, M.; Tansey, K.; Mouillot, F.; Laurent, P.; Storm, T.; Heil, A.; et al. Generation and analysis of a new global burned area product based on MODIS 250 m reflectance bands and thermal anomalies. *Earth Syst. Sci. Data* **2018**, *10*, 2015–2031. [CrossRef]
15. Avetisyan, D.; Velizarova, E.; Filchev, L. Post-Fire Forest Vegetation State Monitoring through Satellite Remote Sensing and In Situ Data. *Remote Sens.* **2022**, *14*, 6266. [CrossRef]
16. Gaveau, D.L.A.; Descals, A.; Salim, M.A.; Sheil, D.; Sloan, S. Refined burned-area mapping protocol using Sentinel-2 data increases estimate of 2019 Indonesian burning. *Earth Syst. Sci. Data* **2021**, *13*, 5353–5368. [CrossRef]
17. García, M.J.L.; Caselles, V. Mapping burns and natural reforestation using thematic Mapper data. *Geocarto Int.* **1991**, *6*, 31–37. [CrossRef]
18. Silva, J.M.N.; Cadima, J.F.C.L.; Pereira, J.M.C.; Grégoire, J.-M. Assessing the feasibility of a global model for multi-temporal burned area mapping using SPOT-VEGETATION data. *Int. J. Remote Sens.* **2004**, *25*, 4889–4913. [CrossRef]
19. Key, C.H.; Benson, N.C. The normalized burn ratio, a Landsat TM radiometric index of burn severity incorporating multi-temporal differencing. In *US Geological Survey*; Northern Rocky Mountain Science Center: Bozeman, MT, USA, 1999.
20. Trigg, S.; Flasse, S. An evaluation of different bi-spectral spaces for discriminating burned shrub-savannah. *Int. J. Remote Sens.* **2001**, *22*, 2641–2647. [CrossRef]
21. Pérez, C.C.; Olthoff, A.E.; Hernández-Trejo, H.; Rullán-Silva, C.D. Evaluating the best spectral indices for burned areas in the tropical Pantanos de Centla Biosphere Reserve, Southeastern Mexico. *Remote Sens. Appl. Soc. Environ.* **2022**, *25*, 100664. [CrossRef]
22. Filipponi, F. BAIS2: Burned Area Index for Sentinel-2. *Proceedings* **2018**, *2*, 364. [CrossRef]
23. Alcaras, E.; Costantino, D.; Guastaferro, F.; Parente, C.; Pepe, M. Normalized Burn Ratio Plus (NBR+): A New Index for Sentinel-2 Imagery. *Remote Sens.* **2022**, *14*, 1727. [CrossRef]
24. Chuvieco, E.; Congalton, R.G. Mapping and inventory of forest fires from digital processing of tm data. *Geocarto Int.* **1988**, *3*, 41–53. [CrossRef]

25. Boschetti, M.; Stroppiana, D.; Brivio, P.A. Mapping Burned Areas in a Mediterranean Environment Using Soft Integration of Spectral Indices from High-Resolution Satellite Images. *Earth Interact.* **2010**, *14*, 1–20. [CrossRef]
26. Giglio, L.; Boschetti, L.; Roy, D.P.; Humber, M.L.; Justice, C.O. The Collection 6 MODIS burned area mapping algorithm and product. *Remote Sens. Environ.* **2018**, *217*, 72–85. [CrossRef] [PubMed]
27. Liu, P.; Liu, Y.; Guo, X.; Zhao, W.; Wu, H.; Xu, W. Burned area detection and mapping using time series Sentinel-2 multispectral images. *Remote Sens. Environ.* **2023**, *296*, 113753. [CrossRef]
28. Veraverbeke, S.; Lhermitte, S.; Verstraeten, W.W.; Goossens, R. Evaluation of pre/post-fire differenced spectral indices for assessing burn severity in a Mediterranean environment with Landsat Thematic Mapper. *Int. J. Remote Sens.* **2011**, *32*, 3521–3537. [CrossRef]
29. Padilla, M.; Stehman, S.V.; Ramo, R.; Corti, D.; Hantson, S.; Oliva, P.; Alonso-Canas, I.; Bradley, A.V.; Tansey, K.; Mota, B.; et al. Comparing the accuracies of remote sensing global burned area products using stratified random sampling and estimation. *Remote Sens. Environ.* **2015**, *160*, 114–121. [CrossRef]
30. Filipponi, F. Exploitation of Sentinel-2 Time Series to Map Burned Areas at the National Level: A Case Study on the 2017 Italy Wildfires. *Remote Sens.* **2019**, *11*, 622. [CrossRef]
31. Giglio, L.; Boschetti, L.; Roy, D.; Hoffmann, A.A.; Humber, M.; Hall, J.V. *Collection 6.1 MODIS Burned Area Product User's Guide Version 1.0*; NASA EOSDIS Land Processes DAAC: Sioux Falls, SD, USA, 2021.
32. Padilla, M.; Van Der Goten, R.; Jacobs, T. *Copernicus Global Land Operations "Vegetation and Energy", "CGLOPS-1" Product User Manual, Burned Area Version 3.1*; Zenodo: Geneve, Switzerland, 2025.
33. Galizia, L.F.; Curt, T.; Barbero, R.; Rodrigues, M. Assessing the accuracy of remotely sensed fire datasets across the southwestern Mediterranean Basin. *Nat. Hazards Earth Syst. Sci.* **2021**, *21*, 73–86. [CrossRef]
34. De Luca, G.; Silva, J.M.N.; Modica, G. Regional-scale burned area mapping in Mediterranean regions based on the multitemporal composite integration of Sentinel-1 and Sentinel-2 data. *Gisci. Remote Sens.* **2022**, *59*, 1678–1705. [CrossRef]
35. Salis, M.; Ager, A.A.; Alcasena, F.J.; Arca, B.; Finney, M.A.; Pellizzaro, G.; Spano, D. Analyzing seasonal patterns of wildfire exposure factors in Sardinia, Italy. *Environ. Monit. Assess.* **2015**, *187*, 4175. [CrossRef]
36. Salis, M.; Arca, B.; Del Giudice, L.; Palaiologou, P.; Alcasena-Urdiroz, F.; Ager, A.; Fiori, M.; Pellizzaro, G.; Scarpa, C.; Schirru, M.; et al. Application of simulation modeling for wildfire exposure and transmission assessment in Sardinia, Italy. *Int. J. Disaster Risk Reduct.* **2021**, *58*, 102189. [CrossRef]
37. Drusch, M.; Del Bello, U.; Carlier, S.; Colin, O.; Fernandez, V.; Gascon, F.; Hoersch, B.; Isola, C.; Laberinti, P.; Martimort, P.; et al. Sentinel-2: ESA's Optical High-Resolution Mission for GMES Operational Services. *Remote Sens. Environ.* **2012**, *120*, 25–36. [CrossRef]
38. Main-Knorn, M.; Pflug, B.; Louis, J.; Debaecker, V.; Müller-Wilm, U.; Gascon, F. Sen2Cor for Sentinel-2. In *Image and Signal Processing for Remote Sensing XXIII*; Bruzzone, L., Bovolo, F., Benediktsson, J.A., Eds.; SPIE: Bellingham, WA, USA, 2017; p. 3. [CrossRef]
39. Roteta, E.; Bastarrika, A.; Franquesa, M.; Chuvieco, E. Landsat and Sentinel-2 Based Burned Area Mapping Tools in Google Earth Engine. *Remote Sens.* **2021**, *13*, 816. [CrossRef]
40. Louis, J.; Devignot, O.; Pessiot, L. *S2 MPC—Level-2A Algorithm Theoretical Basis Document*; European Space Agency: Paris, France, 2021.
41. Zekoll, V.; Main-Knorn, M.; Louis, J.; Frantz, D.; Richter, R.; Pflug, B. Comparison of masking algorithms for sentinel-2 imagery. *Remote Sens.* **2021**, *13*, 137. [CrossRef]
42. CFVA—Perimetri dei Soprassuoli Percorsi dal Fuoco. 2024. Available online: https://webgis2.regione.sardegna.it/geonetwork/srv/ita/catalog.search#/metadata/R_SARDEG:70f50b3a-6dbd-40cf-b1c9-a8c72b764ce6 (accessed on 22 October 2025).
43. Sardegna Geoportale—DTM 10 m. 2025. Available online: https://webgis2.regione.sardegna.it/geonetwork/srv/ita/catalog.search#/metadata/R_SARDEG:JDCBN (accessed on 22 October 2025).
44. Collu, C.; Dessì, F.; Simonetti, D.; Lasio, P.; Botti, P.; Melis, M.T. On the application of remote sensing time series analysis for land cover mapping: Spectral indices for crops classification. *Int. Arch. Photogramm. Remote. Sens. Spat. Inf. Sci.* **2022**, *XLIII-B3-2*, 61–68. [CrossRef]
45. Associazione Italiana di Telerilevamento (AIT) (Ed.) Open Source Technologies for Mapping: Impact Toolbox and the Land Cover Map of Sardinia. In *Earth Observation: Current Challenges and Opportunities for Environmental Monitoring*; AIT Series "Trends in Earth Observation"; Volume 3, Associazione Italiana di Telerilevamento (AIT): Firenze, Italy, 2024; pp. 70–73, ISBN 978-88-944687-2-4. [CrossRef]
46. Trudu, P.L.; Fiori, M.; Peana, I.; Delitala, A. *Rapporto Meteo e Clima 2024*; Regione Autonoma della Sardegna, Assessorato della Difesa dell'Ambiente: Cagliari, Italy, 2024.
47. Del Pilar, M.; Laabal, M.; Sallnaro, E.C. *Cartografía de Grandes Incendios Forestales en la Península Ibérica a Partir de Imágenes Noaa-avhrr*; Universidad de Alcalá de Henares: Madrid, Spain, 1998; Volume 7, pp. 109–128.

48. Benson, N.; Key, C.H. *Landscape Assessment: Ground Measure of Severity, the Composite Burn Index; and Remote Sensing of Severity, the Normalized Burn Ratio*; USDA Forest Service, Rocky Mountain Research Station: Fort Collins, CO, USA, 2006.
49. Sall, B.; Jenkins, M.W.; Pushnik, J. Retrospective analysis of two northern California wild-land fires via Landsat five satellite imagery and Normalized Difference Vegetation Index (NDVI). *Open J. Ecol.* **2013**, *3*, 311–323. [CrossRef]
50. Arisanty, D.; Ramadhan, M.F.; Angriani, P.; Muhaimin, M.; Saputra, A.N.; Hastuti, K.P.; Rosadi, D. Utilizing Sentinel-2 Data for Mapping Burned Areas in Banjarbaru Wetlands, South Kalimantan Province. *Int. J. For. Res.* **2022**, *2022*, 7936392. [CrossRef]
51. Fotakidis, V.; Chrysafis, I.; Mallinis, G.; Koutsias, N. Continuous burned area monitoring using bi-temporal spectral index time series analysis. *Int. J. Appl. Earth Obs. Geoinf.* **2023**, *125*, 103547. [CrossRef]
52. Maskouni, F.H.; Seydi, S.T. Forest Burned Area Mapping Using Bi-Temporal Sentinel-2 Imagery Based on a Convolutional Neural Network: Case Study in Golestan Forest. *Eng. Proc.* **2021**, *10*, 6. [CrossRef]
53. Veraverbeke, S.; Harris, S.; Hook, S. Evaluating spectral indices for burned area discrimination using MODIS/ASTER (MASTER) airborne simulator data. *Remote Sens. Environ.* **2011**, *115*, 2702–2709. [CrossRef]
54. Kaufman, Y.J.; Remer, L.A. Detection of Forests Using Mid-IR Reflectance: An Application for Aerosol Studies. *IEEE Trans. Geosci. Remote. Sens.* **1994**, *32*, 672–683. [CrossRef]
55. Smiraglia, D.; Filipponi, F.; Mandrone, S.; Tornato, A.; Taramelli, A. Agreement index for burned area mapping: Integration of multiple spectral indices using Sentinel-2 satellite images. *Remote Sens.* **2020**, *12*, 1862. [CrossRef]
56. Fawcett, T. An introduction to ROC analysis. *Pattern Recognit. Lett.* **2006**, *27*, 861–874. [CrossRef]
57. Sobrino, J.A. Methodology for burned areas delimitation and fire severity assessment using Sentinel-2 data. A case study of forest fires occurred in Spain between 2018 and 2023. *Recent Adv. Remote Sens.* **2024**, *2*, 1–13. [CrossRef]
58. Marinho Barbosa, P.; Miguel, J.; Pereira, C.; Grégoire, J.-M. *Compositing Criteria for Burned Area Assessment Using Multitemporal Low Resolution Satellite Data*; Elsevier: Amsterdam, The Netherlands, 1993.
59. Gorelick, N.; Hancher, M.; Dixon, M.; Ilyushchenko, S.; Thau, D.; Moore, R. Google Earth Engine: Planetary-scale geospatial analysis for everyone. *Remote Sens. Environ.* **2017**, *202*, 18–27. [CrossRef]
60. Efthimiou, N.; Psomiadis, E.; Panagos, P. Fire severity and soil erosion susceptibility mapping using multi-temporal Earth Observation data: The case of Mati fatal wildfire in Eastern Attica, Greece. *Catena* **2020**, *187*, 104320. [CrossRef]
61. Me, J.; Segarra, D.; Garcia-Hare, J. *Modeling Rates of Ecosystem Recovery after Fires by Using Landsat TM Data*; Elsevier Science Inc.: Amsterdam, The Netherlands, 1997; Volume 61.
62. Morisette, J.T.; Baret, F.; Liang, S. Special Issue on Global Land Product Validation. *IEEE Trans. Geosci. Remote Sens.* **2006**, *44*, 1695–1697. [CrossRef]
63. Boschetti, L.; Roy, D.P.; Justice, C.O. *International Global Burned Area Satellite Product Validation Protocol Part I—Production and Standardization of Validation Reference Data (to be Followed by Part II—Accuracy Reporting)*; Committee on Earth Observation Satellites: Silver Spring, MD, USA, 2009.
64. Pulvirenti, L.; Squicciarino, G.; Negro, D.; Puca, S. Object-Based Validation of a Sentinel-2 Burned Area Product Using Ground-Based Burn Polygons. *IEEE J. Sel. Top. Appl. Earth Obs. Remote Sens.* **2023**, *16*, 9154–9163. [CrossRef]
65. Dice, L.R. Measures of the Amount of Ecologic Association Between Species. *Ecology* **1945**, *26*, 297–302. [CrossRef]
66. Boschetti, L.; Roy, D.P.; Giglio, L.; Huang, H.; Zubkova, M.; Humber, M.L. Global validation of the collection 6 MODIS burned area product. *Remote Sens. Environ.* **2019**, *235*, 111490. [CrossRef]
67. Padilla, M.; Stehman, S.; Litago, J.; Chuvieco, E. Assessing the Temporal Stability of the Accuracy of a Time Series of Burned Area Products. *Remote Sens.* **2014**, *6*, 2050–2068. [CrossRef]
68. McCarley, T.R.; Smith, A.M.S.; Kolden, C.A.; Kreitler, J. Evaluating the Mid-Infrared Bi-spectral Index for improved assessment of low-severity fire effects in a conifer forest. *Int. J. Wildland Fire* **2018**, *27*, 407–412. [CrossRef]
69. Simon Kongo, L. Performance of dNDVI, dNBR and dMIRBI spectral indices in burnt areas detection Case study of Moyowosi game reserve, Kigoma, Tanzania. *Afr. J. Land. Policy Geospat. Sci.* **2025**, *8*, 2657–2664. [CrossRef]
70. Hudak, A.T.; Morgan, P.; Bobbitt, M.J.; Smith, A.M.S.; Lewis, S.A.; Lentile, L.B.; Robichaud, P.R.; Clark, J.T.; McKinley, R.A. The Relationship of Multispectral Satellite Imagery to Immediate Fire Effects. *Fire Ecol.* **2007**, *3*, 64–90. [CrossRef]
71. Luo, H.; Wu, J. An Assessment of the Suitability of Sentinel-2 Data for Identifying Burn Severity in Areas of Low Vegetation. *J. Indian Soc. Remote Sens.* **2022**, *50*, 1135–1144. [CrossRef]
72. Schepers, L.; Haest, B.; Veraverbeke, S.; Spanhove, T.; Vanden Borre, J.; Goossens, R. Burned Area Detection and Burn Severity Assessment of a Heathland Fire in Belgium Using Airborne Imaging Spectroscopy (APEX). *Remote Sens.* **2014**, *6*, 1803–1826. [CrossRef]
73. Hawbaker, T.J.; Vanderhoof, M.K.; Beal, Y.-J.; Takacs, J.D.; Schmidt, G.L.; Falgout, J.T.; Williams, B.; Fairaux, N.M.; Caldwell, M.K.; Picotte, J.J.; et al. Mapping burned areas using dense time-series of Landsat data. *Remote Sens. Environ.* **2017**, *198*, 504–522. [CrossRef]
74. Wang, P.; Zhang, L.; Zhang, G.; Jin, B.; Leung, H. Multispectral Image Super-Resolution Burned-Area Mapping Based on Space-Temperature Information. *Remote Sens.* **2019**, *11*, 2695. [CrossRef]

75. Roy, D.P.; Boschetti, L.; Justice, C.O.; Ju, J. The collection 5 MODIS burned area product—Global evaluation by comparison with the MODIS active fire product. *Remote Sens. Environ.* **2008**, *112*, 3690–3707. [CrossRef]
76. Giglio, L.; Schroeder, W.; Justice, C.O. The collection 6 MODIS active fire detection algorithm and fire products. *Remote Sens. Environ.* **2016**, *178*, 31–41. [CrossRef] [PubMed]